JCTC Journal of Chemical Theory and Computation

Article

pubs.acs.org/JCTC

Probing the Conical Intersection Dynamics of the RNA Base Uracil by UV-Pump Stimulated-Raman-Probe Signals; Ab Initio Simulations

Benjamin P. Fingerhut,* Konstantin E. Dorfman,* and Shaul Mukamel*

Department of Chemistry, University of California, Irvine, California 92697-2025, United States

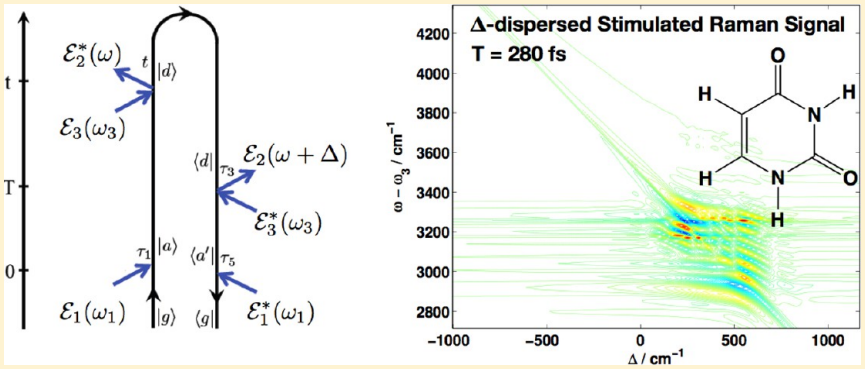

ABSTRACT: Nonadiabatic electron and nuclear dynamics of photoexcited molecules involving conical intersections is of fundamental importance in many reactions such as the self-protection mechanism of DNA and RNA bases against UV irradiation. Nonlinear vibrational spectroscopy can provide an ultrafast sensitive probe for these processes. We employ a simulation protocol that combines nonadiabatic on-the-fly molecular dynamics with a mode-tracking algorithm for the simulation of femtosecond stimulated Raman spectroscopy (SRS) signals of the high frequency C−H- and N−H-stretch vibrations of the photoexcited RNA base uracil. The simulations rely on a microscopically derived expression that takes into account the path integral of the excited state evolution and the pulse shapes. Analysis of the joint time/frequency resolution of the technique reveals a matter chirp contribution that limits the inherent temporal resolution. Characteristic signatures of relaxation dynamics mediated in the vicinity of conical intersection are predicted. The C−H and N−H spectator modes provide high sensitivity to their local environment and act as local probes with submolecular and high temporal resolution.

1. INTRODUCTION

Time- and frequency-resolved vibrational spectroscopy (either with infrared or Raman probes) has long been used to monitor structural rearrangements of atoms. Unique marker bands that serve as fingerprints of excited state photoreactions or nonadiabatic relaxation dynamics allow to resolve transient reaction intermediates with high temporal resolution[1−3] and relate structural changes to the overall reaction mechanism.[4−7] In a typical UV-(or visible) pump-Raman probe experiment, an actinic pump pulse brings the molecule into a valence excited state, thereby launching a photochemical process which is subsequently probed by a delayed Raman pulse sequence. Several variants of spontaneous and stimulated Raman probe techniques which show high temporal and spectral resolution have been reported.[8,9] In a femtosecond stimulated Raman spectroscopy (SRS) experiment, the Raman probe sequence consists of a picosecond pulse $\mathcal{E}_2$ superimposed with a femtosecond laser pulse $\mathcal{E}_3$ which stimulates the Raman signal. Typically, in (off-resonant) SRS, a spectrally resolved pattern of narrow vibrational lines (line width ≈ 10 cm^{-1}) is recorded in short time intervals (20 fs). SRS is thus considered an ideal probe for ultrafast light induced processes[3,10] which relates spectral changes to nuclear rearrangements.

Recently, we have shown that even though the actinic/probe delay time T and the frequency resolution are independent experimental knobs, the SRS signal is indeed limited by the Fourier uncertainty.[11] The relevant range of frequencies that contribute to a given signal is spanned by the matter contribution to the signal, even though the femtosecond Raman probe pulse bandwidth can be much broader. Thus, only some of the probe modes contribute to the signal, and its full bandwidth may become immaterial. The resolution is thus controlled in a nontrivial way by the probe pulse, the measuring device, as well as the system itself by an inherent matter chirp contribution to the signal. Even though the SRS and UV-pump-IR probe techniques involve different physical processes and a different number of field-matter interactions, they share a similar matter contribution to the signal. We have developed a loop diagrammatic approach in the frequency domain that provides a unified description of several state-of-the-art electronically off-resonant Raman techniques,[12] like homodyne-detected frequency-resolved spontaneous Raman spectroscopy, heterodyne-detected time-resolved impulsive stimulated Raman spectroscopy, transient grating impulsive stimu-

Received: November 22, 2013
Published: January 22, 2014

lated Raman spectroscopy, and femtosecond SRS. All signals can be described as six wave mixing experiments and probe the same four-point material correlation function but with different gating windows. We proposed three levels of theory which form a hierarchy of approximations for the simulation of the matter response.[11] The most rigorous and demanding protocol relies on a forward/backward propagation of the system Green's function containing electronic and nuclear degrees of freedom. Further simplifications can be achieved by expanding the matter correlation function in the eigenstates of the joint nuclear/electronic space. The third most intuitive semiclassical protocol only retains the quantum character of a few nuclear degrees of freedom which are modulated in a classical bath. Gaussian fluctuations can be conveniently accounted for by using the second order cumulant expansion. Recently, we implemented the semiclassical protocol to predict IR-probe signatures of C═O modes of uracil.[13] The simulations revealed that the technique can distinguish different excited state relaxation channels on a femtosecond time scale.

In this paper, we extend the previous work on uracil to predict ab intio derived time-resolved SRS signals of high frequency C−H- and N−H-stretch vibrations which serve as spectator modes. SRS provides a higher time-resolution than IR. We will demonstrate that the high-frequency C−H modes are especially sensitive to the structural changes accompanying the relaxation process and thus serve as local probes for out-of-plane distortions of the π system. Characteristic SRS signatures of conical intersection (CoIn) mediated relaxation events can be identified on the single trajectory level as well as in the ensemble averaged signal, making the technique a sensitive probe for the concurrent relaxation mechanisms. The employed nonadiabatic on-the-fly molecular dynamics (NA-O-MD) semiclassical simulation protocol allows one to follow the ultrafast relaxation dynamics mediated by CoIn's. C−H and N−H vibrational modes are treated quantum mechanically while the rest constitute a bath which modulates the observed frequencies during the course of the ultrafast nonadiabatic relaxation dynamics. The molecular quantities are obtained from microscopic NA-O-MD[14,15] in full coordinate space. The quantum character of the normal modes is recovered by a mode tracking procedure[16] which scales linearly with the number of considered spectator modes and makes the protocol particularly suited for blocks of isolated high frequency modes. Since the numerical effort does not scale directly with system size, this allows for simulations of excited states of medium-sized molecules where the full excited state Hessian is not accessible. If other modes are close in energy and mix during the photoreaction, the more rigorous and expensive direct propagation protocol must be used.

The microscopically derived signal expressions for the SRS technique involve a path integral of the molecule excited state evolution and may not be interpreted as a snapshot of the molecular dynamics.[17] The inherent temporal and spectral resolution is analyzed on the basis of the Δ-dispersed signal[12] revealing a matter chirp contribution to the signals. The interpretation of the signals thus requires a careful analysis of the interplay between spectral and temporal resolution of the excited state time-resolved vibrational spectra.[3,4,18]

The intense UV absorption bands of DNA and RNA nucleobases lead to the population of bright valence excited states with $\pi\pi^*$ character. In nature, the electronic energy is converted into vibrational energy on a femtosecond to picosecond time scale, thus minimizing harmful photochemical processes. This conical-intersection-mediated self-protection mechanism against UV irradiation is under active study.[19,20] Competing molecular dimerization leading to photochemical DNA lesions has been shown to occur on a comparable, few picosecond time scale,[2] affected by variations of the base sequence and the conformation double helix.[21−24] Time resolved optical techniques (UV or visible pump−probe or photoelectron spectroscopy) and their multidimensional optical counterparts[25−27] offer a high sub-100 fs temporal resolution.[28,29] The broad bandwidth of the optical or ionizing probe pulses erodes the spectral selectivity of the underlying vibrational dynamics, and monitoring the population decay of the bright $\pi\pi^*$ state requires elaborate modeling of dark states, which complicates the analysis.

The excited state lifetimes of the isolated pyrimidine bases are a few picoseconds (with the longest for thymine) with subpicosecond kinetic contributions.[30,31] The excited state deactivation proceeds along several interconnected excited state decay pathways:[32−34] a direct $\pi\pi^* \rightarrow$ gs channel leads to ultrafast repopulation of the electronic ground state,[28,29,31,35] while an indirect $\pi\pi^* \rightarrow n_O\pi^* \rightarrow$ gs channel involves an optical dark $n_O\pi^*$ intermediate state with a longer lifetime.[31] Even though simulations of DNA and RNA bases demonstrated the interconnection between the two relaxation mechanisms and additional minor ring-opening pathways, the relative importance of these pathways is still under debate.[36−39] Spectroscopic signatures were reported[36] only for the earliest stages of the relaxation process.

2. THE UV-PUMP STIMULATED-RAMAN PROBE SIGNAL

In stimulated Raman spectroscopy (SRS), an actinic pump pulse initiates the vibrational dynamics in the excited electronic state. The Raman probe consists of a picosecond pulse $\mathcal{E}_3$ and a femtosecond pulse $\mathcal{E}_2$, and the signal is given by frequency-dispersed probe transmission $\mathcal{E}_2(\omega)$. We consider electronically off resonant SRS described by the level scheme and diagrams depicted in Figure 1a,b. From the intuitive diagrammatic representation, we note that the SRS signal is treated in the joint matter/field space involving six field−matter interactions and that the matter response enters as a four-point material correlation function. The detection mode is defined by the frequency dispersed detection windows of the $\mathcal{E}_2$ probe pulse. We treat the electronically off-resonant Raman process induced by pulses $\mathcal{E}_2$ and $\mathcal{E}_3$ process as instantaneous and describe it by the effective field/matter interaction Hamiltonian:

$$H'(t) = \alpha_n \, \mathcal{E}_2^{\dagger}(t) \, \mathcal{E}_3(t) + \mathcal{E}_1^{\dagger}(t) \, V_e(t) + H.\,c. \tag{1}$$

where the excited state polarizability which couples fields $\mathcal{E}_2$ and $\mathcal{E}_3$ parametrically via a symmetric (real) operator $\alpha_n = \bar{\alpha}_n + \bar{\alpha}_n^{\dagger}$, and $V_e(t)$ denotes the electronic transition dipole moment. For the narrow band pulse $\mathcal{E}_3$, we set $\mathcal{E}_3(t - T) = \mathcal{E}_3 \, e^{-i\omega_3(t-T)}$. The frequency-gated Raman signal at delay time T can then be expressed in the form

$$S_{SRS}(\omega - \omega_3, T) = \mathcal{I} \int_{-\infty}^{\infty} \frac{d\Delta}{2\pi} \, \mathcal{E}_2^*(\omega) \, \mathcal{E}_2(\omega + \Delta) \, \tilde{S}_{SRS}(\omega - \omega_3, T; \Delta) \tag{2}$$

where $\omega - \omega_3$ denotes the Raman shift and $\mathcal{I}$ denotes the imaginary part. The experimental observable $S_{SRS}(\omega - \omega_3, T)$

dx.doi.org/10.1021/ct401012u | J. Chem. Theory Comput. 2014, 10, 1172−1188

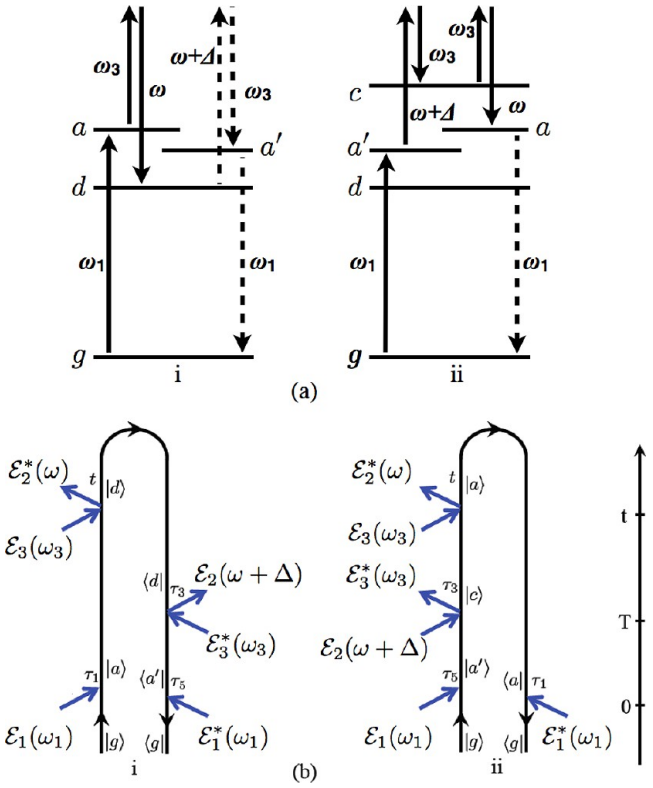

Figure 1. (a) Level scheme and (b) loop diagrams of the off-resonant stimulated Raman spectroscopy (SRS) technique. Time translation invariance yields $\omega_1 + \omega_3 - \omega + (\omega + \Delta) - \omega_3 - \omega_1 = 0$. The signal is given by these diagrams plus their complex conjugate.

is obtained by integration over the Δ variable of the Δ-dispersed signal $\tilde{S}_{SRS}(\omega - \omega_3, T; \Delta)$ subject to the influence of the femtosecond probe field $\mathcal{E}_2(\omega + \Delta)$.

The Δ-dispersed signal[12] can be readily read from the two diagrams of Figure 1b:

$$\tilde{S}_{SRS}(\omega - \omega_3, T; \Delta) = \tilde{S}^{(i)}_{SRS}(\omega - \omega_3, T; \Delta) + \tilde{S}^{(ii)}_{SRS}(\omega - \omega_3, T; \Delta) \quad (3)$$

$$\tilde{S}^{(i)}_{SRS}(\omega - \omega_3, T; \Delta) = \frac{2}{\hbar}\int_{-\infty}^{\infty} dt \int_{-\infty}^{t} d\tau_1 \int_{-\infty}^{t} d\tau_3 \int_{-\infty}^{\tau_3} d\tau_5 |\mathcal{E}_3|^2 \mathcal{E}_1^*(\tau_5) \times \mathcal{E}_1(\tau_1)\langle V_e G^\dagger(\tau_3, \tau_5)\, \alpha_n G^\dagger(t, \tau_3)\, \alpha_n G(t, \tau_1) V_e^\dagger\rangle\, e^{i(\omega-\omega_3)(t-\tau_3) - i\Delta(\tau_3 - T)} \quad (4)$$

$$\tilde{S}^{(ii)}_{SRS}(\omega - \omega_3, T; \Delta) = \frac{2}{\hbar}\int_{-\infty}^{\infty} dt \int_{-\infty}^{t} d\tau_1 \int_{-\infty}^{t} d\tau_3 \int_{-\infty}^{\tau_3} d\tau_5 |\mathcal{E}_3|^2 \mathcal{E}_1(\tau_5) \times \mathcal{E}_1^*(\tau_1)\langle V_e G^\dagger(t, \tau_1)\, \alpha_n G(t, \tau_3)\, \alpha_n G(\tau_3, \tau_5)\, V_e^\dagger\rangle\, e^{i(\omega-\omega_3)(t-\tau_3) - i\Delta(\tau_3 - T)} \quad (5)$$

Here, $G(t_1, t_2) = (-i/\hbar)\theta(t_1 - t_2)\, e^{-iH(t_1 - t_2)}$ is the retarded Green's function that represents forward time evolution with the free-molecule Hamiltonian H. $G^\dagger$ represents backward time evolution. Equations 4 and 5 can be interpreted as a forward and backward time evolving vibronic wave packet arising from the interactions of diagram i and ii of Figure 1, respectively. For diagram i, moving along the loop clockwise, pulse $\mathcal{E}_1$ first excites the molecule to an excited state via $V^\dagger$. The wave function then propagates from time τ_1 until t, where the Raman sequence de-excites the system to a lower vibrational level d via the polarizability α_n. Followed by a backward propagation from t to τ_3, re-excitation of the wavepacket to a' occurs in a Raman process. After backward propagation from τ_3 to τ_5, the final de-excitation by pulse $\mathcal{E}_1$ brings the system back to the initial state $|g\rangle$. Similarly, in diagram ii, two successive forward propagations (τ_5 to τ_3 and τ_3 to t) which involve excitation and de-excitation to a higher vibrational level c are followed by a backward propagation of the wavepacket from time t to τ_1. The corresponding four point correlation functions $\langle V_e G^\dagger(\tau_3, \tau_5)\, \alpha_n G^\dagger(t, \tau_3)\, \alpha_n G(t, \tau_1) V_e^\dagger\rangle$ and $\langle V_e G^\dagger(t, \tau_1)\, \alpha_n G(t, \tau_3)\, \alpha_n G(\tau_3, \tau_5) V_e^\dagger\rangle$ contain all relevant matter information for any frequency and time-domain Raman technique.[12] By assuming impulsive UV excitation, we can set $\mathcal{E}_1(\tau) = \mathcal{E}_1\delta(\tau)$ and eliminate the τ_1 and τ_5 integrals.

Even though the Δ-dispersed signal (eqs 4 and 5) is not an experimental observable, it facilitates the analysis and interpretation of SRS signals. While the narrow band picosecond component corresponds to $\mathcal{E}_3$ and enters as amplitude square, the femtosecond probe field $\mathcal{E}_2$ affects both the detection axis ω and the Δ axis as it enters as $\mathcal{E}_2^*(\omega)\, \mathcal{E}_2(\omega + \Delta)$. $\tilde{S}_{SRS}(\omega - \omega_3, T; \Delta)$ contains all matter information relevant for the signal which spans the required probe bandwidth of $\mathcal{E}_2$ along the Δ axis. Δ thus represents the relevant range of $\mathcal{E}_2$ frequencies that affect the signal. Equations 2−5 demonstrate that the actual contributing range of frequencies to the SRS signal is spanned by the variable Δ. If the $\mathcal{E}_2$ bandwidth is sufficiently broad, its actual value becomes immaterial and does not improve the time resolution of the SRS measurement. The resolution is therefore jointly controlled by the probe pulse, the measuring device, as well as the system dynamics under investigation.

2.1. Semiclassical off-Resonant Stimulated Raman Signal. A more intuitive simplified description can be developed by including only some of the vibrational degrees of freedom as quantum variables while treating the majority degrees of freedom as a classical bath. The trajectories of instantaneous frequencies $\omega(t)$, together with the respective dipole moments μ_{ag} and polarizabilities $\alpha_{\nu\nu'}$, then fully define the matter contribution to the SRS signal. Taking the UV-pulse as impulsive ($\mathcal{E}_1(t) = \mathcal{E}_1\delta(t)$), we get

$$\tilde{S}_{SRS}(\omega - \omega_3, T; \Delta) = -\frac{2i}{\hbar^4}\int_{-\infty}^{\infty} dt \int_{-\infty}^{t} d\tau_3\, |\mathcal{E}_1|^2 |\mathcal{E}_3|^2\, e^{i(\omega-\omega_3)(t-\tau_3)} \times e^{-i\Delta(\tau_3 - T)} \sum_a |\mu_{ag}|^2\, e^{-\gamma_a(t+\tau_3)} \left[\sum_c \alpha_{ac}^2\, e^{-i\int_{\tau_3}^{t} \omega_{ac}(t')dt'} - \sum_d \alpha_{ad}^2\, e^{+i\int_{\tau_3}^{t} \omega_{ad}(t')dt'} \right] \quad (6)$$

The instantaneous frequencies $\omega(t)$ enter eq 6 via a path integral; the signal thus depends on the entire pathway from time T to the time when the polarization decays to zero. Additionally, eq 2 fully accounts for probe pulse effects beyond the impulsive limit. Ensemble averaging $\langle ... \rangle_e$ over a classical set of trajectories must be performed on the signal level $S_{SRS}(\omega - \omega_3, T)$. Equation 2 can also be used to simulate spectra of a

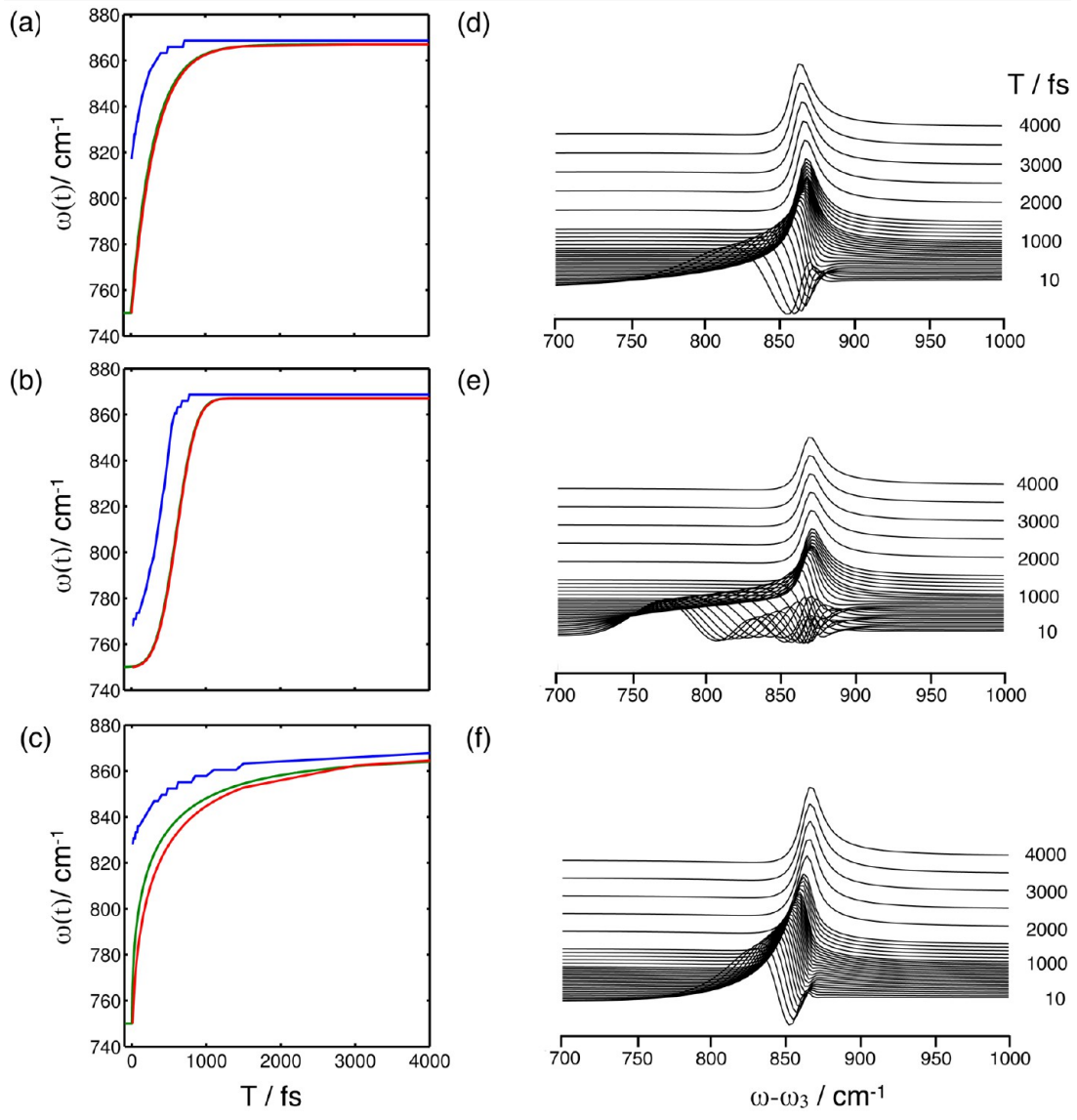

Figure 2. Instantaneous frequencies $\omega(t)$ (a–c, green lines) and corresponding SRS signals (d–f) for different model kinetics: (a) exponential change of $\omega(t)$; (b) Gaussian error-function model characterized by $\sigma_{system} = 1/\Gamma$; (c) stretched exponential change of $\omega(t)$. In all simulations, the initial frequency ω_i is set to 750 cm^{-1}, and the final frequency ω_f is set to 867 cm^{-1}. Dephasing rate: $1/\gamma_{ac} = 1/620$ fs and the rate of frequency change $\Gamma = 1/325$ fs. For the stretched exponential, a β parameter of 0.5 was used in the simulations. Blue lines follow the maximum of the SRS peak position, and red lines correspond to the integrated peak area.

single molecule[40,41] by looking at a single trajectory. If we assume that the fluctuations satisfy Gaussian statistics, we can evaluate the ensemble average via the second order cumulant expansion.[11] This does not apply to the current system; instead we perform a numerical ensemble average of eq 2 to obtain the observable signal.

2.2. Signatures of Model System Kinetics in SRS Signals. Before presenting the SRS signal obtained from ab initio dynamics of photoexcited uracil, we briefly discuss simplified kinetic models. This will help clarify how the actual time constants and the time dependent vibrational frequencies appear in the signals. Figure 2a–c depict the time evolution of a single vibrational mode $\omega(t)$ using three kinetic models (green lines; the model parameters are given in the caption). If the system follows ordinary first-order kinetics, the change in the instantaneous frequency $\omega(t)$ is described by a single exponential (Figure 2a), with rate Γ. For relaxation dynamics in the vicinity of CoIn's, the simple first-order kinetics does not apply, and stepwise population transfer is observed.[29,42−45] We model this with a Gaussian error function characterized by the time scale $\sigma_{system} = 1/\Gamma$ (green line in Figure 2b; for details of the model, see caption and ref 11). A third system dynamics scenario involves stretched exponential kinetics (green line in Figure 2c). This typically arises from inhomogenous initial populations, distributions of reactive distances, or the coupling to a slow collective coordinate.[46−48]

The resulting SRS signals for the three models are depicted in Figure 2d–f. The SRS signal of the exponential model shows a dispersive line shape at early time ($T\Gamma < 1$) with a pronounced maximum at detection frequencies $\omega - \omega_3$ above $\omega_i = 750$ cm^{-1} even at early times, which evolve to the final frequency $\omega_f = 867$ cm^{-1} for later times T with a purely absorptive line shape (Figure 2d). Thus, the short time spectra are dominated by a mixed absorptive plus dispersive peak for ω_i with a weak dispersive contribution from ω_f. As T is increased, the dispersive features decay exponentially and a single

dx.doi.org/10.1021/ct401012u | J. Chem. Theory Comput. 2014, 10, 1172−1188

absorptive resonance at ω_f survives. In the SRS signal of the CoIn model, we observe a complex pattern consisting of absorptive and dispersive line shapes at early delay times (Figure 2e, $T\Gamma < 1$). On the basis of this, one could incorrectly assume that multiple vibrational modes appear at early delay times which reduce into a single resonance at $\omega_f = 867$ cm^{-1} for large T. In the case of the stretched exponential model, we observe a SRS signal similar to the ordinary exponential case with initially dispersive line shapes which gradually evolves toward $\omega_f = 867$ cm^{-1} for large T (Figure 2f). The width of the dispersive peak is reduced compared to the pure exponential dynamics case.

Together with the instantaneous frequency evolution $\omega(t)$ (green lines), we depict the derived system dynamics from the SRS signals in Figure 2a−c. By following the maximum of the SRS signal (blue lines), we see that for all three models the apparent system kinetics in SRS is faster than the real system kinetics, an effect already observed for a snapshot limit formulation of the SRS signal.[49] In the exponential and stretched exponential model (Figure 2a and c) even at the earliest times the maximum peak positions start around 820 cm^{-1} and evolve toward the final frequency $\omega_f = 867$ cm^{-1}. In the CoIn model (Figure 2b), the initial value of $\omega(t)$ is also not recovered, even though the deviations are smaller than in both other kinetics cases. Thus, following the maximum peak position in SRS spectra gives an incomplete picture of the time evolution of $\omega(t)$ and the associated system dynamics due to the interference of absorptive and dispersive line shapes at early times. In contrast, by following the integrated peak area (red lines), the system dynamics can be fully recovered for the exponential and CoIn model (Figure 2a and b). In the stretched exponential model (Figure 2b), the real system dynamics cannot be fully recovered from the integrated peak shift; nevertheless, close agreement can be achieved (compare the green and red lines in Figure 2f).

A better understanding of how SRS peak shapes are affected by system dynamics with varying T can be obtained from analogy with the effect of phase functions on Fourier limited ultrashort pulses in pulse shaping experiments.[50] A Fourier limited pulse modulated by a quadratic or higher order phase function in the Fourier plane acquires a chirp, and the resulting frequency domain envelope function is altered. In SRS, the line shape subject to the pure vibrational dephasing corresponds to the Fourier limited signal. The system dynamics acts as a phase function imposed by the matter which alters the signal line shape. As the signal may not be recast as an amplitude square of the transition amplitude,[12] the symmetry between both branches of the loop is broken, giving rise to dispersive line shapes. First order kinetics appears as an exponential phase function. Extracting the instantaneous frequency (i.e., the system dynamics) from SRS signals is equivalent to a reconstruction of the phase function of the signal.

3. THE SEMICLASSICAL SIMULATION PROTOCOL

The main steps in the microscopic simulation protocol of SRS signals in the semiclassical approximation (eq 6) involve molecular dynamics simulations subject to nonadiabatic relaxation over conical intersections, the reconstruction of an excited state effective vibrational Hamiltonian from classical dynamics to obtain trajectories of instantaneous frequencies $\omega_{\nu\nu'}(t)$, and the evaluation of the mode specific Raman intensities. The numerical realization of all steps will be outlined below, computational details are given in a separate subsection.

3.1. Nonadiabatic On-the-Fly Molecular Dynamics (NA-O-MD). In NA-O-MD simulations, the nuclei are treated classically and follow Newton's equations of motion.[51,52] The nuclei's acceleration $\ddot{R}$ is given by the gradient of the respective potential of the populated electronic state i

$$\ddot{R} = -\frac{1}{M}\frac{\partial E^{S_i}(R)}{\partial R} \tag{7}$$

The forces on the nuclei $\partial E^S_i(R)/\partial R$ are evaluated by solving the time-independent Schödinger equation for the electrons and a subsequent gradient calculation based on the Ehrenfest theorem.[51,53] The time dependent electronic population is described by the electronic expansion coefficients $c_{k/j}$, which follow the equation of motion:

$$i\hbar\dot{c}_k = \sum_j c_j(V_{kj} - i\hbar\dot{R}\cdot d_{kj}(R)) \tag{8}$$

Changes in electronic populations are thus defined by the velocity vector $\dot{R}$, given by the PES gradient (see eq 7) and the potential energy matrix V_{kj}. In the adiabatic representation, V_{kj} is diagonal. The derivative coupling vector

$$d_{kj}(R) = \left\langle \Phi_k(r;R) \middle| \frac{\partial}{\partial R} \middle| \Phi_j(r;R) \right\rangle \tag{9}$$

with $\Phi_k(r;R)$ and $\Phi_j(r;R)$ being the adiabatic wave functions of states k and j, depends parametrically on the position of the nuclei R. The transition probability can be evaluated by the scalar product $\dot{R}\cdot d_{kj}(R)$. A balanced description of the gradients $\partial E^S_i(R)/\partial R$ and derivative coupling vectors $d_{kj}(R)$ for several electronic states is thus the basic requirement of NA-O-MD. An excellent overview over the theoretical methods suitable for NA-O-MD simulations is given in ref 52. The present NA-O-MD simulations of the RNA base uracil use the *Newton-X* program package,[14,15] where surface hopping between different electronic states is described by Tully's surface hopping algorithm.[51] All electronic structure calculations used to obtain excitation energies, excited state gradients, and derivative coupling vectors were carried out with the MOLPRO program package.[54]

3.2. Time-Dependent Instantaneous Frequencies $\omega_{\nu\nu'}(t)$. The NA-O-MD simulations yield trajectories of the electronic state potential energies $E_i(t)$ together with the evolving nuclear geometries $q(t)$ as classical objects. We focus on the time-evolution of the Raman active high frequency C−H- and N−H-stretch vibrations which show spectator character along the reaction coordinate. The course of the trajectories is evaluated with a $\delta t = 1$ fs time step by the mode tracking algorithm (for details see below). The normal modes are evaluated along the trajectory, over the entire normal mode coordinate space of the C−H and N−H vibrations, i.e., the inner turning point, the equilibrium structure, and the outer turning point. This yields a highly oscillating function $\omega(q(t))$ which contains the dependence on the position of the normal mode coordinate (see dashed lines in Figures 4 and 5)

In order to obtain the instantaneous C−H and N−H vibrational frequencies during the nonadiabatic dynamics, we note that fast oscillation occurs around the equilibrium structure q_0 of the normal mode defined as the arithmetic mean. q_0 evolves in time due to nonadiabatic relaxation. To extract the instantaneous vibrational frequency $\omega_{\nu\nu'}(t)$, we

apply a second-order Butterworth filter to $\omega(q(t))$, which is designed to have a frequency response as flat as possible in the passband. Compared to Chebyshev or Elliptic filters, the Butterworth filter rolls off more slowly around the cutoff frequency ω_{cutoff}, but minimizes the jitter of $\omega(t)$. The passband frequency was empirically adjusted to 133.4 cm^{-1}. Compared to the linear filter used for the simulation of UV-pump-IR probe signals in ref 13, the employed Butterworth filter yields a much smoother instantaneous frequency response which can be gradually tuned by varying the passband frequency. As SRS involves an impulsive detection mode (see discussion in section 4.3.1), a jitter in $\omega(q(t))$ directly translates into a jitter of the SRS signal which is eventually averaged out in the ensemble averaged signal. Whether modulations in $\omega(t)$ on the time scale of vibrational periods can be observed in single molecule experiments[40,41] is an exciting future direction, which can be directly addressed by variations ω_{cutoff}. Anticorrelated beating of certain modes in $\omega(q(t))$ which are neglected and damped by the filtering can be exploited to derive couplings between normal modes, as required for the simulation of multidimensional extensions of SRS measurements. IR probe measurements, in contrast, inherently average over $\omega(q(t))$[13] as the IR probe field is longer or comparable to the period of the vibrational frequency.[1,2]

For calculating the C−H and N−H stretch vibrations over the course of the trajectories, we adopt an instantaneous normal mode (INM) approach[55,56] which was extensively used to study low frequency intermolecular vibrations in liquids and intramolecular high-frequency spectator modes[57−59] (i.e., the C−H and N−H motions). The Hessian matrix, i.e. the matrix of second derivatives of the energy with respect to nuclear coordinates is evaluated at nonequilibrium configurations, and the resulting frequencies are partitioned into stable (real) eigenvalues and unstable (imaginary) eigenvalues. The high-frequency spectator modes are modulated by all other nuclear bath motions and possess stable (real) eigenvalues due to their spectator character along the reaction coordinate. Application of the protocol to low frequency skeleton motions can be questionable as they can potentially evolve between stable and unstable modes. The full quantum propagation of the Green's function according to eqs 4 and 5 will then be required.

Mode Tracking. The standard INM approach involves the diagonalization of the full (mass-wheighted) Hessian matrix (within the harmonic approximation) at every time step yielding $3N$ eigenvalues and eigenvectors for a molecule containing N atoms

$$(\mathbf{H}^{(m)} - \lambda_i)L_i = 0 \tag{10}$$

with $\lambda_i \propto \omega_i^2$ being the eigenvalues of the ith vibrational frequency. To follow the excited state dynamics of specific "fingerprint" modes (e.g., the C−H- and N−H-stretch vibrations), a block-diagonal Hessian can be constructed in an iterative subspace Davidson procedure,[16] avoiding the calculation of the full excited state Hessian. In brief, in the mode tracking algorithm, the solution of eq 10 is avoided and is formally replaced by

$$(\mathbf{H}^{(m)} - \lambda_i^{(k)})L_i^{(k)} = r_i^{(k)} \tag{11}$$

where $r_i^{(k)}$ is the residuum vector in iteration k for the approximate eigenvector $L_i^{(k)}$. The numerical procedure starts with a collective displacement b_i of all atoms for each considered normal mode. The first basis vector serves as an initial guess. In consecutive iterations, the normal mode eigenvectors are expanded by the generation of new basis vectors out of the residuum until convergence. By calculating the numerical derivative of the gradient of the electronic energy with respect to the basis vector $\mathbf{b}$, the vectors σ_i are determined by

$$\sigma_i = \mathbf{H}^{(m)} b_i \tag{12}$$

and used to generate the small Davidson matrix $\tilde{\mathbf{H}}$ with elements

$$\tilde{H}_{ji} = b_j^T \mathbf{H}^{(m)} b_i = b_j^T \sigma_i \tag{13}$$

Diagonalization of $\mathbf{H}^{(m)}$ yields the approximate eigenvectors $L_i^{(k)}$ and eigenvalues $\lambda_i^{(k)}$ of iteration k together with the residuum vector $r_i^{(k)}$ (eq 11). The desired vibration is selected in a root homing procedure by comparing and following the mode with the largest overlap with the initial guess vector(s). The mode tracking protocol exploits the fact that the important modes of the simulated spectrum are known *a priori* without the need to calculate all $3N - 6$ vibrational frequencies, omitting all unnecessary modes. This decouples the numerical effort from system size. The full Hessian matrix, which is the most time-consuming step in the standard quantum chemical procedure, is not required.

Equation 6 assumes that the "fingerprint" modes are independent, each undergoing its own fluctuations. In the mode tracking procedure,[16] all modes are naturally treated as independent normal modes (i.e., diagonalization of the Hamiltonian with time varying couplings is avoided). During the iterative procedure, localized normal modes are provided as a guess; diagonalizing the small Davidson Hessian in a time-varying basis yields orthogonal modes which allow access to the vibrational Hamiltonian $H_{\text{nuc}}(t)$ in diagonal form. The localized character of two C−H or N−H vibrations is preserved during the dynamics, justifying the use of eq 6.

3.3. Raman Intensities. The Raman intensities α^2 are expressed in terms of Raman Scattering factors $\mathcal{L}$ within the double harmonic approximation:[60,61]

$$\mathcal{L} = 45a'^2_k + 7\gamma'^2_k \tag{14}$$

where a'^2_k and γ'^2_k are the derivatives of the hermitian polarizability tensor $\bar{\alpha}$ with respect to the kth normal mode.

$$a'_k = \frac{1}{3}[(\overline{\alpha'_{xx}})_k + (\overline{\alpha'_{yy}})_k + (\overline{\alpha'_{zz}})_k] \tag{15}$$

$$\begin{aligned}\gamma'_k = {} & \frac{1}{2}[(\overline{\alpha'_{xx}})_k - (\overline{\alpha'_{yy}})_k]^2 + \frac{1}{2}[(\overline{\alpha'_{yy}})_k - (\overline{\alpha'_{zz}})_k]^2 \\ & + \frac{1}{2}[(\overline{\alpha'_{zz}})_k - (\overline{\alpha'_{xx}})_k]^2 + 3[(\overline{\alpha'_{xy}})_k^2 + (\overline{\alpha'_{yz}})_k^2 \\ & + (\overline{\alpha'_{zx}})_k^2]\end{aligned} \tag{16}$$

Here, $(\overline{\alpha}'_{rs})_k$ denotes the derivatives of the polarizability tensor components with respect to the collective kth normal mode displacement vector q_k

$$(\overline{\alpha'_{rs}})_k = \frac{\partial \overline{\alpha}_{rs}}{\partial q_k} \text{ with } r, s = x, y, z \tag{17}$$

The polarizability tensor components $\bar{\alpha}_{rs}$ are given by the partial derivatives of the electronic energy E_{el} with respect to a static electric field $\mathcal{E}_{r/s}$

$$\bar{\alpha}_{rs} = -\left(\frac{\partial^2 E_{el}^0}{\partial \mathcal{E}_r \partial \mathcal{E}_s}\right) \quad (18)$$

We assume observation parallel to a linearly y-polarized incoming laser beam irradiating the sample and propagating along the z axis. Scattered light is detected in the $y-z$ plane (forward scattering for stimulated Raman signals, scattering angle $\theta = 0$). Different experimental geometries can be accounted for using the relations given in ref 60.

3.4. Computational Details. *Nonadiabatic On-the-Fly Molecular Dynamics (NA-O-MD).* The Velocity-Verlet algorithm[62] with a time step $\Delta t = 0.5$ fs is used for the integration of classical equations of motions of the nuclei with the *Newton-X* program package.[14] Within this interval, a reduced time step of $\Delta t/20$ is used to interpolate the energy gradients and derivative coupling vectors for a continuous update of the electronic population.[14,63] The unitary propagator is used for the integration of the electronic Schrödinger equation to account for time-reversal symmetry around the loop, which is not guaranteed for the fifth order Butcher algorithm.[64] During the dynamics of the individual trajectories, the derivative coupling vectors are evaluated between neighboring electronic states; the phase of the derivative coupling vector is followed to avoid phase jumps during the dynamics. After a hopping event between electronic states, the momentum of the nuclei is adjusted along the direction of the derivative coupling vectors to conserve the total energy. To investigate the femtosecond relaxation dynamics of the RNA base uracil, an uncorrelated Wigner distribution of the electronic ground state was sampled, and 76 trajectories were generated for the NA-O-MD simulations. As an impulsive pulse is assumed for the UV photoexcitation, all trajectories are chosen without imposing further restrictions on the excitation energies. If only a certain frequency window is accessible due to the finite bandwidth of the excitation pulse, the procedure described in ref 37 can be applied.

Electronic Structure Calculations. In all simulations, the electronic structure of the RNA base uracil is treated at the CASSCF level. All π orbitals as well as the two lone pairs (n_{O_7}, n_{O_8}) are included in the active space. The resulting CAS(14/10) wave function (CAS(m/n) with m being the number of active electrons and n being the number of active orbitals) allows for a description of all relevant electronic states, namely the electronic ground state (S_0), the optical accessible $\pi\pi^*$ state, and two dark states, which correspond to excitations from the n_{O_7} and n_{O_8} lone pairs into antibonding π^* orbitals ($n_{O_7}\pi^*$, $n_{O_8}\pi^*$). The simulations start in the optical bright $\pi\pi^*$ state (depending on the initial condition either S_2 or S_3) and include the four electronic states S_0, S_1 ($n_O\pi^*$), S_2 ($\pi\pi^*$), and S_3 ($n_O\pi^*$) during the dynamics, resulting in a *state average* (= *sa*)-CASSCF wave function without symmetry restrictions with four equally weighted states (*sa4*-CAS(14/10)).

In the Franck–Condon (FC) region, the CASSCF excitation energies of the $\pi\pi^*$ state are too high due to the lack of dynamic electron correlation (see Table 1).[37,65−67] Nevertheless, the main characteristics of the excited state potential energy surfaces (minima, conical intersection, and reaction pathways) are reasonably described, as has been investigated in extensive benchmark calculations on uracil using MRCI[37] and MRPT2[36] levels of theory. Interestingly, the barriers to reach the conical intersection on the excited state potential energy surface are well described by CASSCF, allowing the reproduction of experimental time constants[37,68] without a significant speedup of the reaction dynamics. The 6-31G* basis set is used in all dynamic calculations.

Table 1. Excitation Energies of Uracil (in eV)[a]

state	CAS(14/10)	MRPT2	character	exp.[b]	theor.[c]
		sa4-CAS(14/10)			
1A′	−412.528 85	−413.609 07	π		
2A′	6.61	5.07	$\pi\pi^*$ (H → L)	5.1	5.25
1A″	5.14	4.90	$n_O\pi^*$ (n_O → L)		5.00
2A″	6.69	6.37	$n_O\pi^*$ (n_O → L + 1)		
		sa6-CAS(14/10)			
1A′	−412.527 35	−413.613 64	π		
2A′	6.62	5.12	$\pi\pi^*$ (H → L)	5.1	5.25
3A′	7.28	6.00	$\pi\pi^*$ (H+1 → L)		
4A′	8.62	6.63	$\pi\pi^*$ (H → L + 1)		
1A″	5.11	4.96	$n_O\pi^*$ (n_O → L)		5.00
2A″	6.69	6.40	$n_O\pi^*$ (n_O → L + 1)		

[a]The absolute energy of the electronic ground state is given in Hartrees, B3LYP optimized structure with *Cs* symmetry, basis: 6-31G*. [b]Maximum of vapor spectrum.[73] [c]CR-EOM-CCSD(T)/aug-cc-pVTZ[74]

Additional quantum chemical calculations have been performed to take into account the dynamic part of the electron correlation (see Table 1). The calculations use the *MS*-MRPT2[69,70] level of theory and serve as a benchmark for vertical excitation energies. In all *MS*-MRPT2-CAS(14/10) calculations, a level shift $s = 0.3$[71] has been applied. As the energies of the S_1 and S_2 excited electronic states are within 0.2 eV (see Table 1), a multistate treatment of the dynamic electron correlation is required.

Mode Tracking. Mode tracking is performed over the course of the trajectories for both C−H and N−H stretch vibrations of uracil with the Akira program[16] coupled to the MOLPRO program package[54] by a developed interface allowing for mode tracking in excited states by the supplied analytic excited state energy gradients. As an initial guess, C−H and N−H stretch normal mode vectors of the stationary points of the respective populated electronic state at time t are supplied. To guarantee convergence of the desired C−H and N−H modes, root homing is performed by following the eigenvector with the largest overlap with the initial guess vector during the iterative procedure. The numerical derivative of the gradient of the electronic energy of the respective electronic state is evaluated for a displacement of step size 0.01 bohr.[61] For preconditioning, an initial guess unity matrix $\mathbf{X} = \mathbf{1}$ is supplied. For the iterative procedure, the convergence criteria are 0.0005 as maximum component of residuum vector $r_i^{(k)}$ and 0.5×10^{-7} for the change of the maximum component of $r_i^{(k)}$.

Numerical Evaluation of the Polarizability Tensor Derivatives. The polarizability tensor components $\bar{\alpha}_{rs}$ are evaluated by numerical differenciation of E_{el}^0 by using a three-point central difference Bickley formula with an applied static field strength of 0.001 a.u. to the one electron Hamiltonian.[72] The diagonal tensor components are given by

$$\bar{\alpha}_{rr} = -\left(\frac{\partial^2 E_{el}^0}{\partial \mathcal{E}_r \partial \mathcal{E}_r}\right) \approx \frac{E_{el}^+ + E_{el}^- - 2E_{el}^0}{(\mathcal{E}_r^+ - \mathcal{E}_r^0)(\mathcal{E}_r^- - \mathcal{E}_r^0)} \quad (19)$$

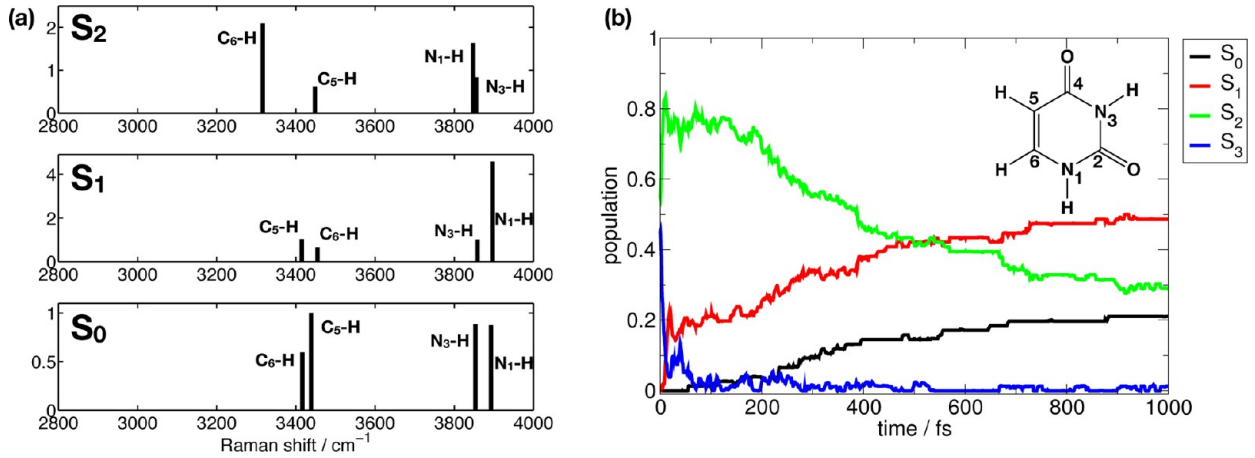

Figure 3. (a) Spontaneous Raman spectrum of the electronic ground state S_0 (bottom), the first excited state S_1 (middle), and the second excited state S_2 (top) calculated at the CASSCF(14/10) level of theory. (b) Electronic population averaged over the set of 76 trajectories. The inlay shows the chemical structure of uracil.

where $\mathcal{E}_r^{+/-}$ denotes the static electric field in the forward or backward direction of r, respectively, and $E_{el}^{+/-}$ denotes the respective electronic energies with applied electric field.

The off-diagonal tensor components are evaluated according to

$$\bar{\alpha}_{rs} = -\left(\frac{\partial^2 E_{el}^0}{\partial\mathcal{E}_r\partial\mathcal{E}_s}\right) \approx \frac{E_{el}^{+,+} - E_{el}^{+,-} - E_{el}^{-,+} + E_{el}^{-,-}}{4(\mathcal{E}_r^+ - \mathcal{E}_r^0)(\mathcal{E}_s^- - \mathcal{E}_s^0)} \quad (20)$$

Here, $E_{el}^{+,+/-,-/+,-/-,+}$ denote the electronic energies with applied electric fields in positive (negative) r and s directions.

The polarizability tensor $\bar{\alpha}_{rs}$ is subsequently differentiated numerically with respect to the normal mode displacement vector q_k (eq 17) obtained from the iterative mode tracking procedure (three-point central differences Bickley formula with a step size 0.01 a.u.). A systematic increase in accuracy can be achieved by using five-point or higher central differences.

For the simulation of SRS signals, we approximate the Raman intensities by neglecting the nuclear coordinate dependence (Franck−Condon approximation) while taking into account the relative intensity of vibrational modes in the different populated electronic excited states. Non-Codon effects can be incorporated by numerical differentiation of the excited state polarizabilities with respect to the "fingerprint" normal modes q_i along the trajectory, followed by the filtering procedure described in section 3.2.

4. RESULTS AND DISCUSSION

4.1. Electronic Excited States and Stationary Vibrational Spectra of Uracil. At the C_s symmetric ground state equilibrium structure of uracil, the lowest optical accessible electronic state of A′ symmetry has $\pi\pi^*$ character and is 6.61 eV above the ground state at the CAS(14/10) level of theory. Taking dynamic electron correlation effects into account at the MRPT2 level, the $\pi\pi^*$ state is further stabilized by ∼1.5 eV (see Table 1), allowing for good agreement with the experimental excitation energy. Two dark $n_O\pi^*$ states are considered (1A″ and 2A″) whose energies are 5.14 and 6.69 eV at the CAS(14/10) level of theory and less sensitive to electron correlation effects. It has been shown by Hudock et al.[36] (MRPT2) and Nachtigallova et al.[37] (MRCI) that CASSCF is adequate for the excited state dynamics of uracil. Even though the $\pi\pi^*$ state shows strong sensitivity to dynamic electron correlation effects, the electronic state order is preserved, and the relative energetics of the excited state potential energy surfaces and geometries of stationary points are reproduced.

Figure 3a shows the stationary spontaneous Raman spectrum of C−H- and N−H-stretch vibrations (calculated according to eqs 14−18) of the electronic ground state minimum S_0, the first excited state minimum S_1 (with $n_O\pi^*$ character), and the localized minimum of the S_2 state (with $\pi\pi^*$ character and characterized by a significant out-of-plane distortion of the hydrogen atom at C_6[36]). In S_0, both pairs of modes have comparable intensity and the splitting due to the different chemical environment of N−H-stretch vibrations is somewhat larger than the splitting of C−H-stretch vibrations. Upon photoexcitation into the bright S_2 state, the splitting of the C−H modes is increased. The splitting of the N−H modes, in contrast, is reduced in the S_2 state. In the dark S_1 state, the splitting and intensity pattern of C−H modes is similar to the electronic ground state S_0, while N−H stretch vibrations now obey a characteristic intensity modulation.

4.2. Population Dynamics of Uracil. The NA-O-MD electronic populations eventually define the observed dynamics in the simulated $S_{SRS}(\omega - \omega_3, T)$ signals of single trajectories and in the averaged ensemble. In Figure 3c, we present the mean electronic population averaged over a set of 76 trajectories, where the electronic structure is computed at the CAS(14/10) level, considering the complete π system as well as both n_O lone pairs in the active space of electrons. The dynamics starts in the bright $\pi\pi^*$ state (due to the close state succession, either S_2 (55.3%) or S_3 (44.7%)). Ultrafast population redistribution occurs within the first 20 fs, leading to an intermediately stable S_1 population of about 20% and S_2 population of ∼72% until 190 fs. Hereafter, the S_2 state with $\pi\pi^*$ character is depopulated, leading to a stable S_2 population of ∼30% at t = 1 ps. The derived lifetime of the $\pi\pi^*$ state is 516 fs (single exponential fit), in good agreement with the 530 fs time constant reported by Ullrich et al. from time-resolved photoelectron measurements.[30] Both S_0 and S_1 show a population increase up to 21.1% and 48.7% at t = 1 ps, respectively. Interestingly, the increase in the combined S_0 and S_1 population in the interval [190; 1000] fs coincides with the decay of the bright S_2 state, which accordingly serves as a reservoir for two relaxation channels. The first channel leads to the population of a dark S_1 state (denoted as $\pi\pi^* \rightarrow n_O\pi^*$

dx.doi.org/10.1021/ct401012u | J. Chem. Theory Comput. 2014, 10, 1172−1188

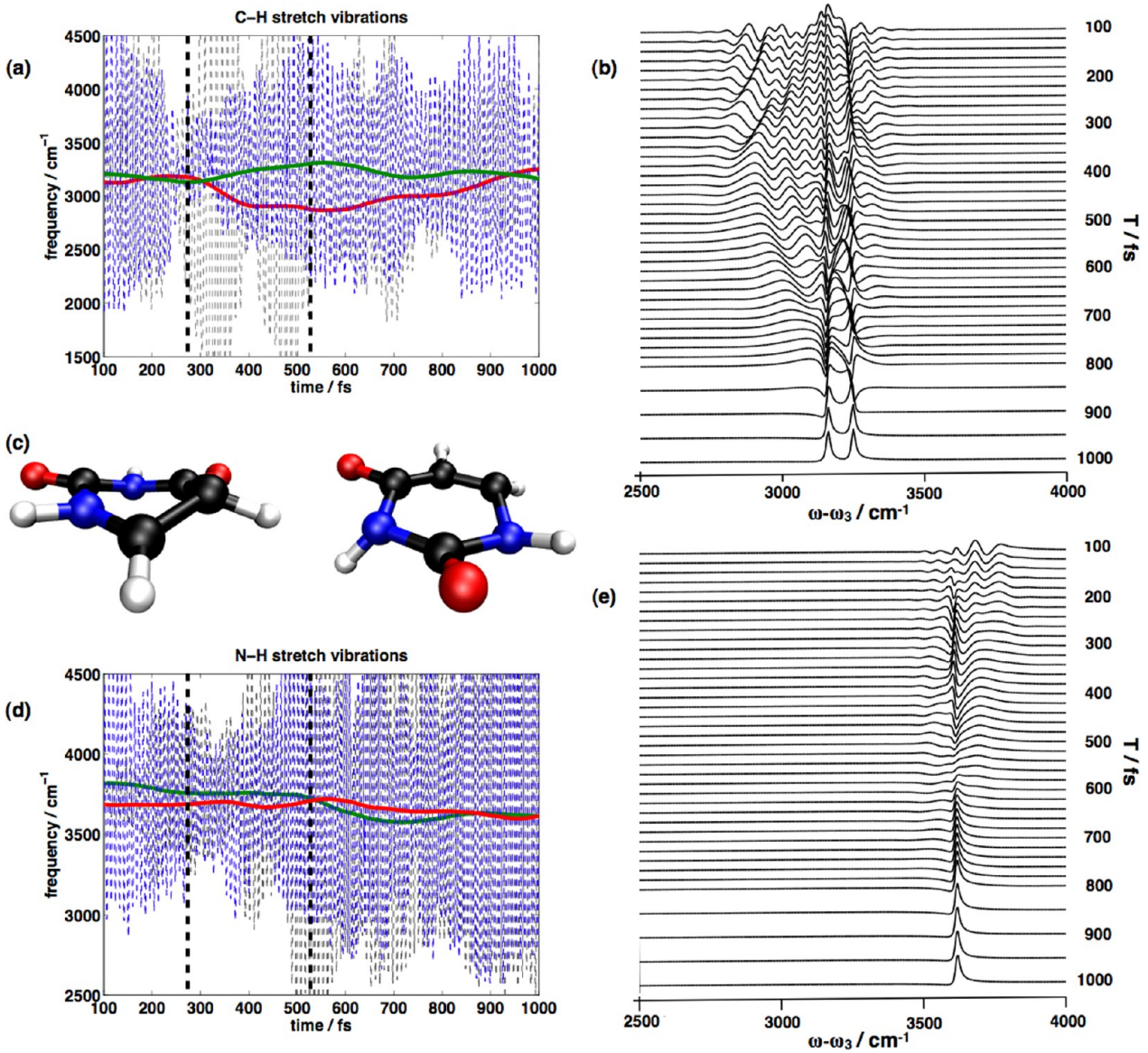

Figure 4. (a) Instantaneous frequencies of C−H stretch vibrations of a prototype trajectory showing $\pi\pi^* \rightarrow n_O\pi^*$ relaxation. (b) SRS signal (eq 2) of C−H stretch vibrations (simulated according to eq 6). (c) Snapshots of the molecular dynamics at t = 270 fs (left) and t = 526 fs (right). Carbon atoms are colored in black, nitrogen atoms in blue, oxygen atoms in red, and hydrogen atoms in white. (d) Instantaneous frequencies of N−H stretch vibrations. (e) SRS signal (eq 2) of N−H stretch vibrations.

relaxation), while in the second channel the excited state population is funneled into the ground state and converted into vibrational excess energy. Inspection of the individual trajectories reveals that the population of the electronic ground state involves two consecutive nonadiabatic hopping events. Initially, $S_2 \rightarrow S_1$ relaxation occurs, where population follows the diabatic $\pi\pi^*$ character, followed by $S_1 \rightarrow S_0$ relaxation (data not shown). The intermediate time in the S_1 state varies between 8 and 59 fs, which does not increase the transient S_1 population in Figure 3c. This relaxation channel is denoted as *diabatic* $\pi\pi^*_{S_2} \rightarrow \pi\pi^*_{S_1} \rightarrow$ gs relaxation.

In summary, our NA-O-MD simulations confirm the mechanistic picture proposed by Hudock et al.[36] where two pathways from the FC point dictate the relaxation dynamics, either (1) relaxation toward an S_2 minimum from where *diabatic* $\pi\pi^*_{S_2} \rightarrow \pi\pi^*_{S_1} \rightarrow$ gs relaxation can occur or (2) relaxation into S_1 mediated by a S_2/S_1 CoIn. CAS(14/10) simulations indicate a stronger participation of the $n_O\pi^*$ state in the relaxation process compared to ref 36. Nachtigallová and co-workers[37] proposed additional excited-state relaxation pathways of uracil, an indirect channel which involves $n_O\pi^* \rightarrow$ gs relaxation and a ring-opening pathway. We found $n_O\pi^* \rightarrow$ gs decay only for t > 1 ps in a minor set of two trajectories. The ring-opening pathway was observed for three trajectories, corresponding to 6% of all ground state hopping events. The Lischka group[75] had extensively studied the effect of varying active space sizes on the importance of distinct relaxation pathways. Analysis of our CAS(14/10) results suggests that the additional fully bonding π orbital predominantly stabilizes the electronic ground state and increases its energy gap to the $n_O\pi^*$ state (the $n_O\pi^*$ state is 5.14 eV above the electronic ground state at the CAS(14/10) level, compared to 4.84 eV at the CAS(10/8) level[37]). The propensity of $n_O\pi^* \rightarrow$ gs relaxation is then reduced, leading to a trapped $n_O\pi^*$ population subsequent to initial $\pi\pi^* \rightarrow n_O\pi^*$ population transfer. As a side effect, the

dx.doi.org/10.1021/ct401012u | J. Chem. Theory Comput. 2014, 10, 1172−1188

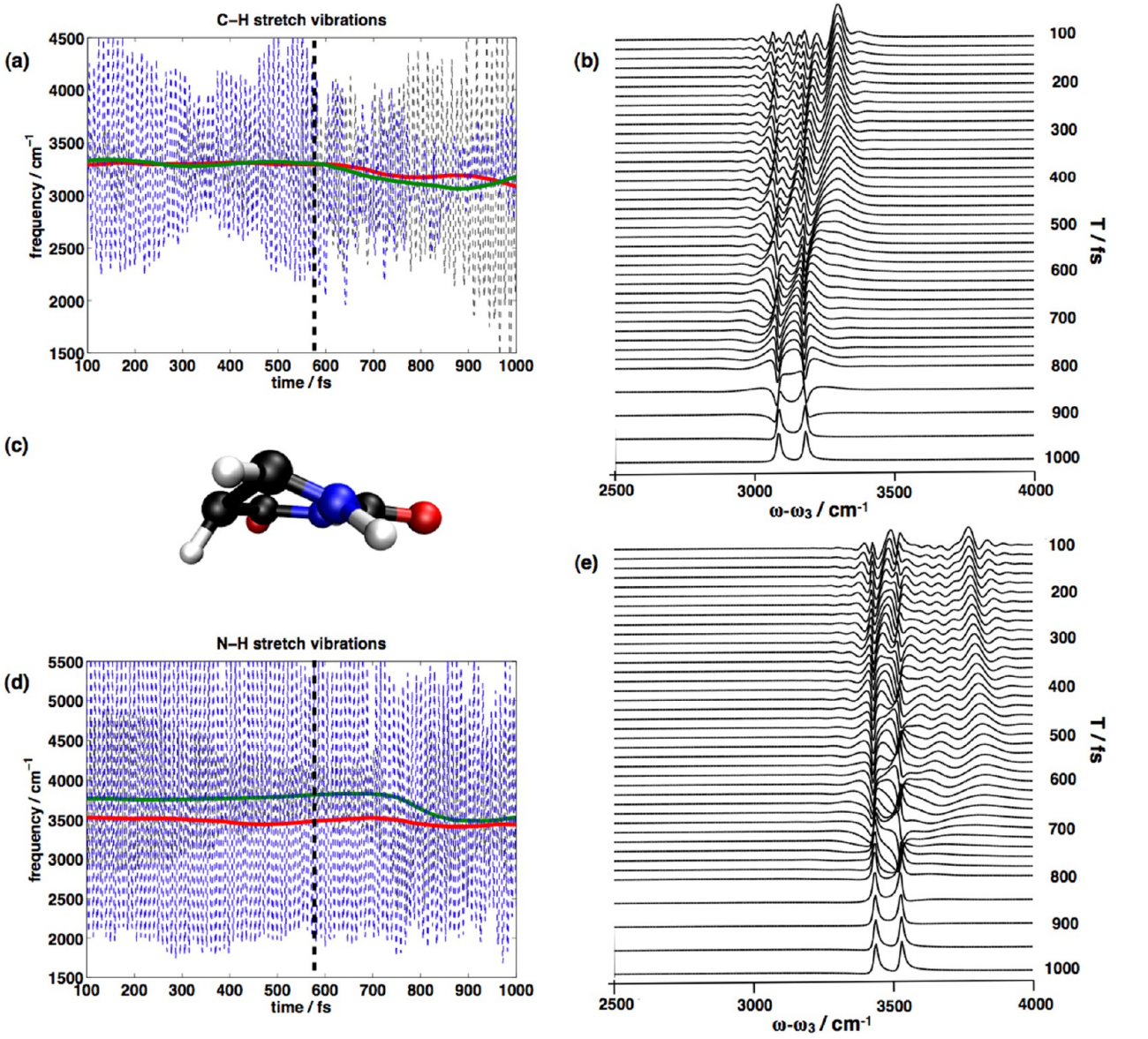

Figure 5. (a) Instantaneous frequencies of C−H stretch vibrations of a prototype trajectory showing *diabatic* $\pi\pi^*_{S_2} \rightarrow \pi\pi^*_{S_1} \rightarrow$ gs relaxation. (b) SRS signal (eq 2) of C−H stretch vibrations (simulated according to eq 6). (c) Snapshot of the molecular dynamics at t = 586 fs. (d) Instantaneous frequencies of N−H stretch vibrations. (e) SRS signal (eq 2) of N−H stretch vibrations.

S_3 state with $n_O\pi^*$ character could facilitate (and overestimate) $\pi\pi^* \rightarrow n_O\pi^*$ population transfer, resulting in a reduced $\pi\pi^*$ population. Asturiol et al. compared dynamic simulations at the CASSCF level of theory with static CASPT2 calculations on thymine and concluded that the propensity of the decay of the $n_O\pi^*$ state could be overestimated in the CASSCF dynamics.[34] Time-resolved transient absorption measurements[31] indicate a participation of the $n_O\pi^*$ state of 10−50% (with 28% for U) in the $\pi\pi^*$ decay, where the dark state has a lifetime of 10−150 ps, in agreement with the present simulations. Additional simulations with longer propagation times and ideally considering dynamic electron correlation effects[76] will be required to quantitatively resolve the importance of the parallel relaxation mechanisms.

In the following, we analyze the SRS signatures of different relaxation channels in order to facilitate for experimental assignments.

4.3. SRS Signals of Uracil. *4.3.1. Instantaneous C−H and N−H Frequencies and SRS Signal on the Single Trajectory Level.* Figure 4 depicts the time- and frequency-resolved SRS signal of C−H- and N−H-stretch vibrations of uracil for a typical trajectory showing $\pi\pi^* \rightarrow n_O\pi^*$ relaxation, together with the instantaneous frequencies $\omega(t)$ derived from NA-O-MD simulations. The ab initio data of the INM analysis for both modes, containing the nuclear dependence $q(t)$, i.e. $\omega(q(t))$, are given as dashed lines. We start by analyzing the signatures of C−H stretch modes (Figure 4a,b). This trajectory shows a $\pi\pi^* \rightarrow n_O\pi^*$ hopping event at t = 270 fs. The time-evolution of instantaneous frequencies $\omega(t)$ reveals that subsequent to the hopping event the C−H spectator modes adjust to the new charge distribution of the populated $n_O\pi^*$ state. This leads to a splitting of C−H frequencies, which has its origin predominantly from a red shift of the C_6−H mode (red line in Figure 4a). Inspection of the trajectory geometries reveals a strong tendency toward $sp^2 \rightarrow sp^3$ rehybridization at

dx.doi.org/10.1021/ct401012u | J. Chem. Theory Comput. 2014, 10, 1172−1188

C_6 subsequent to $\pi\pi^* \rightarrow n_O\pi^*$ relaxation (Figure 4c), which weakens the C_6−H mode potential and induces the observed red shift. The C−H stretch modes thus serve as valuable probes of rearrangements within the ring structure by retaining their spectator character along the reaction coordinate. Due to energy redistribution within the molecule, a slow adjustment toward equilibrium frequencies of the populated electronic state occurs. During the dynamics (t > 500 fs), the tendency for $sp^2 \rightarrow sp^3$ rehybridization at C_5 increases, which leads to a gradual red shift of the C_5−H mode (green line in Figure 4a) and reduces the splitting of the two C−H vibrations.

In the SRS signal of C−H-stretch vibrations (Figure 4b), the dynamics of the red-shifted C_6−H mode appears as transient resonance at $\omega-\omega_3 \approx 3000$ cm^{-1}. Compared to the resonances at T = 1 ps whose line-width is determined by the vibrational dephasing time scale γ = 620 fs, the SRS signal of the C_6−H mode is substantially broadened and shows dispersive line shapes on the blue edge of the resonance. Both the broadening and the characteristic line shape represent the phase function imposed by the matter dynamics. Similarly, the dynamics of the C_5−H mode appears at higher frequencies ($\omega-\omega_3 \approx 3300$ cm^{-1}) as matter-chirp broadened resonance and evolves for T > 500 fs toward the doublet of both C−H stretch vibrations. Interestingly, already at early delay times (T = 200−300 fs), a complex interference pattern appears at the values of final C−H frequency, a consequence of the path integral in eq 6. This again demonstrates that the SRS signal may not be viewed as a snapshot of the instantaneous frequencies $\omega(t)$.

The instantaneous frequencies $\omega(t)$ of N−H-stretch vibrations together with the calculated SRS signal are presented in Figure 4d,e. Due to the hopping event at t = 270 fs, both N−H vibrations gradually evolve from higher frequencies ($\omega(t$ = 300 fs) = 3800 cm^{-1}) toward lower frequencies ($\omega(t$ = 1 ps) = 3600 cm^{-1}), while the splitting of both modes is decreased and becomes small compared to the overall frequency shift. Comparison with the spontaneous Raman spectrum (Figure 3a) reveals that the vibrations appear red-shifted, as due to the excess energy in the S_1 state, the anharmonic region of the potential is probed in the INM approach. By inspection of trajectory geometries, we can correlate the red shift of both N−H-stretch vibrations with an increased tendency of rehybridization at N_1 and N_3 during the dynamics (Figure 4c), as expected for the S_1 minimum structure with out-of-plane displacement of N_3−H.[77] Again, both stretching vibrations serve as a local probe, allowing one to follow structural rearrangements within the pyrimidone core. The gradual change in the N−H instantaneous frequencies directly translates into a pseudoexponential behavior in the simulated SRS signal (Figure 4e). As the splitting of the two modes is smaller than the change in frequency and the vibrational dephasing, only a single resonance appears in $S_{SRS}(\omega-\omega_3, T)$. Initially, the resonance is broadened by the matter-chirp contribution with dispersive features on the red edge. With increasing delay time, the N−H resonances evolve toward their final value around $\omega-\omega_3 \approx$ 3550 cm^{-1} and substantially narrow, eventually reflecting the vibrational dephasing time scale. Again, the maximum peak position does not reflect the actual instantaneous frequency $\omega(t)$ (compare Figure 2 and the discussion in section 2.2).

The instantaneous C−H stretch vibrations of a typical trajectory of *diabatic* $\pi\pi^*_{S_2} \rightarrow \pi\pi^*_{S_1} \rightarrow$ gs relaxation are depicted in Figure 5a together with the respective SRS signal (b). In this trajectory, the nonadiabatic relaxation event into the ground state occurs at t = 586 fs. The relevant CoIn structure exhibits a strong out-of-plane displacement of the C_6−H fragment together with substantial rehybridization at C_5 accompanied by a pronounced out-of-plane displacement of C_5−H. In the time evolution of instantaneous C−H vibrations, the structural rearrangements are reflected by a red shift of both modes for t > 600 fs. Since rehybridization at C_5 induces a stronger change in local potential, the red shift of the C_5−H mode is more pronounced and the splitting of both C−H modes is increased (see green line in Figure 5, left). Both C−H modes show an instantaneous response (within 10 fs) in their induced frequency changes at the CoIn structure.

In the SRS signal of C−H modes of *diabatic* $\pi\pi^*_{S_2} \rightarrow \pi\pi^*_{S_1} \rightarrow$ gs relaxation (Figure 5b), a single, system dynamics broadened resonance with dispersive line shape appears initially. Due to the frequency shift induced by nonadiabatic relaxation, this resonance evolves toward lower frequencies ($\omega-\omega_3 \approx 3100$ cm^{-1}) with complex shape for T > 550 fs. Since the two modes spectrally overlap (with anticorrelated frequency shifts), the new spectral feature shows characteristic dispersive line shapes on both the red and blue edge of the resonance. A further increase of T leads to a splitting of both C−H mode resonances which evolve toward a Lorentzian line shape. As both modes are direct local probes to changes, especially at the C_5 position which are required to reach the CoIn, the SRS signal nearly instantaneously resembles the system dynamics. The extent to which this CoIn specific spectral signature survives in the ensemble averaged SRS signal will be discussed in section 4.4.

In contrast to the C−H modes, the N−H SRS response is delayed by about 150 fs to the actual passage of the CoIn (Figure 5d). As can be seen from the instantaneous evolution of N−H modes, only the N_1−H mode shows a significant response to the new charge distribution while the N_3−H evolution shows only weak modulations. For passage through the CoIn, C_6 adjacent to N_1 is significantly displaced out of the ring plain (Figure 5c). Accordingly, changes in charge distribution appear more significant at N_1 than N_3. In the SRS signal of N−H modes (Figure 5e), two spectrally separated resonances appear at early delay times T, where only the higher frequency N_1−H mode is broadened due to the system dynamics imposed chirp contribution. With increasing T, the high frequency resonance decays ($T \approx$ 800 fs) and the SRS signal evolves into two sharp resonances around $\omega-\omega_3$ = 3500 cm^{-1} whose line width eventually represents the vibrational dephasing time scale. At intermediate times, a complex spectral pattern appears between both resonances, which closely resembles the model dynamics of Figure 2. The stepwise change in the instantaneous vibrational frequency of the N_1−H mode closely resembles the model kinetics of a Gaussian error function.

In summary, we have demonstrated that the SRS signals of C−H- and N−H-stretch vibrations serve as sensitive local probes of complex CoIn mediated dynamics. The C−H modes which are adjacent to structural rearrangements required for the passage of CoIn structures show an instantaneous response, while the ground state relaxation pathway is delayed in the SRS signal of the more remote N−H stretch vibrations. Characteristic SRS patterns of nonexponential dynamics were identifed at least at the single trajectory level, which could serve as a sensitive probe for stepwise population dynamics mediated by CoIns.

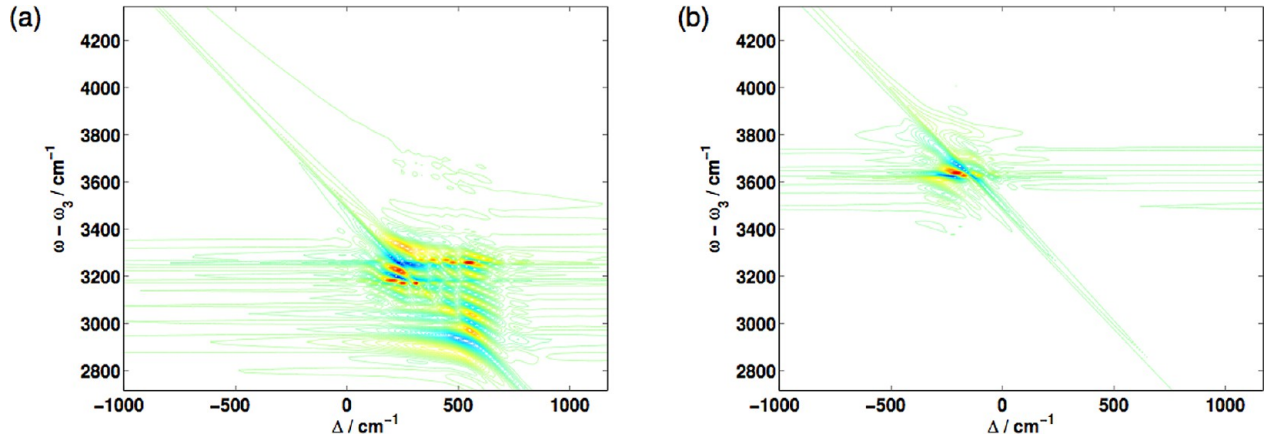

Figure 6. (a) Δ-dispersed signal (eq 3) of C−H-stretch vibrations of $\pi\pi^* \rightarrow n_O\pi^*$ relaxation; T = 280 fs. (b) Δ-dispersed signal (eq 3) of N−H-stretch vibrations; T = 280 fs.

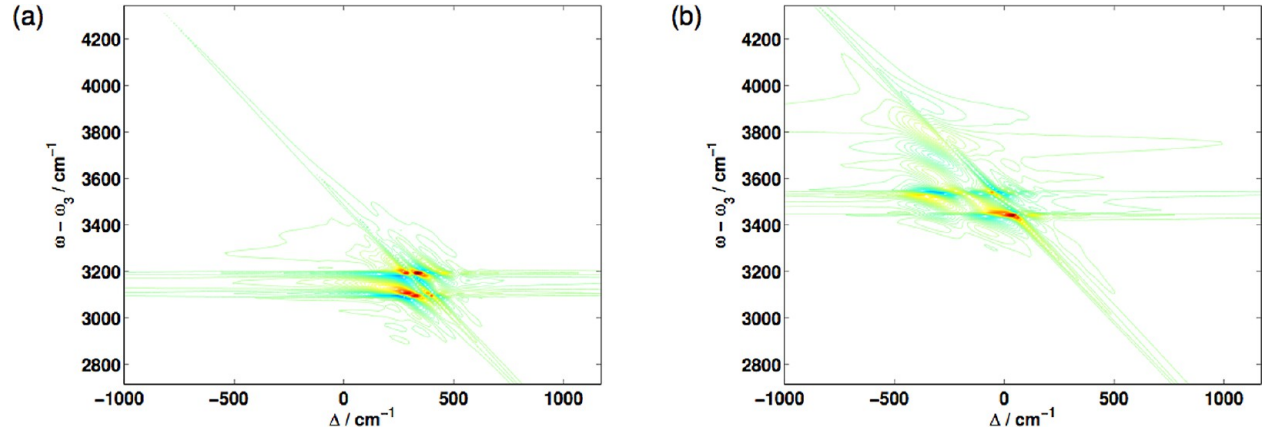

Figure 7. (a) Δ-dispersed signal (eq 3) of C−H-stretch vibrations of *diabatic* $\pi\pi^*_{S_2} \rightarrow \pi\pi^*_{S_1} \rightarrow$ gs relaxation; T = 580 fs. (b) Δ-dispersed signal (eq 3) of N−H- stretch vibrations relaxation; T = 580 fs.

4.3.2. The Δ-Dispersed Signal: What Is the Genuine Time and Frequency Resolution of the SRS Technique. The Δ-dispersed signal (eq 6) contains more information than the experimental signal and clearly demonstrates the conjugate time-frequency resolution inherent to SRS experiments. The signal is given by integration over the Δ axis (eq 2). Two alternative and intuitive joint time/frequency signal representations are given in the Appendix. Both in the Wigner and von Neuman representation,[78] not only does the probe pulse act in one of the conjugate time or frequency domains but its action in the plane of the conjugate variables ω_n and t_m is revealed, showing the contribution of the $(\omega_n t_m)$ component of the probe field to the signal detected at $\omega-\omega_3$ and T.

In Figure 6a, we present the Δ-dispersed signal of C−H stretch vibrations for T = 280 fs of the trajectory of $\pi\pi^* \rightarrow n_O\pi^*$ relaxation. Along the detection axis $(\omega-\omega_3)$, the resonances of the SRS signal at the observation time T can be identified. Note that due to the path integral over the instantaneous frequency $\omega(t)$ in eq 6, the resonances along $\omega-\omega_3$ do not represent a snapshot of the system dynamics (compare Figure 4b). All frequency components contributing to a single mode in $\omega-\omega_3$ are revealed along the Δ axis. As the instantaneous frequencies $\omega(t)$ of the C_6−H and C_5−H mode show either an increase or a decrease in their respective values (see Figure 4a), both positive and negative frequency components enter along the Δ axis, and the Δ dispersed signal appears symmetric along the diagonal, giving rise to a matter-induced upchirp and downchirp contribution to the SRS signal. Figure 6b shows the Δ-dispersed signal (eq 3) of N−H stretch vibrations at T = 280 fs. As both modes show decreased instantaneous frequency values at later times, the Δ dispersed signal appears asymmetric along the diagonal, representing the downchirp contribution to the SRS signal. Similarly, the Δ dispersed signal of both, the C−H and N−H vibrations of the trajectory of *diabatic* $\pi\pi^*_{S_2} \rightarrow \pi\pi^*_{S_1} \rightarrow$ gs relaxation (Figure 7a,b) appear asymmetric along the diagonal as the evolution of instantaneous frequencies is dominated by a decrease in frequency subsequent to the hopping event.

The 2D-representation of the Δ-dispersed signal reveals that SRS signals are indeed limited by the Fourier uncertainty in their respective conjugate variables. Even though along the detection axis $\omega-\omega_3$ high frequency resolution can be obtained, high temporal resolution affects the signal along the not observable Δ axis, where the high bandwidth of the fs probe pulse selects the contributing frequency components. Both the $\omega-\omega_3$ axis and the Δ axis are controlled by independent experimental knobs. The inherent matter chirp contribution defines the required bandwidth of the probe ω_3. As the probe pulse becomes much broader, only limited frequency components of the pulse contribute to the signal, and the probe bandwidth becomes irrelevant. On the other hand, the probe bandwidth has to cover the bandwidth spanned by the

dx.doi.org/10.1021/ct401012u | J. Chem. Theory Comput. 2014, 10, 1172−1188

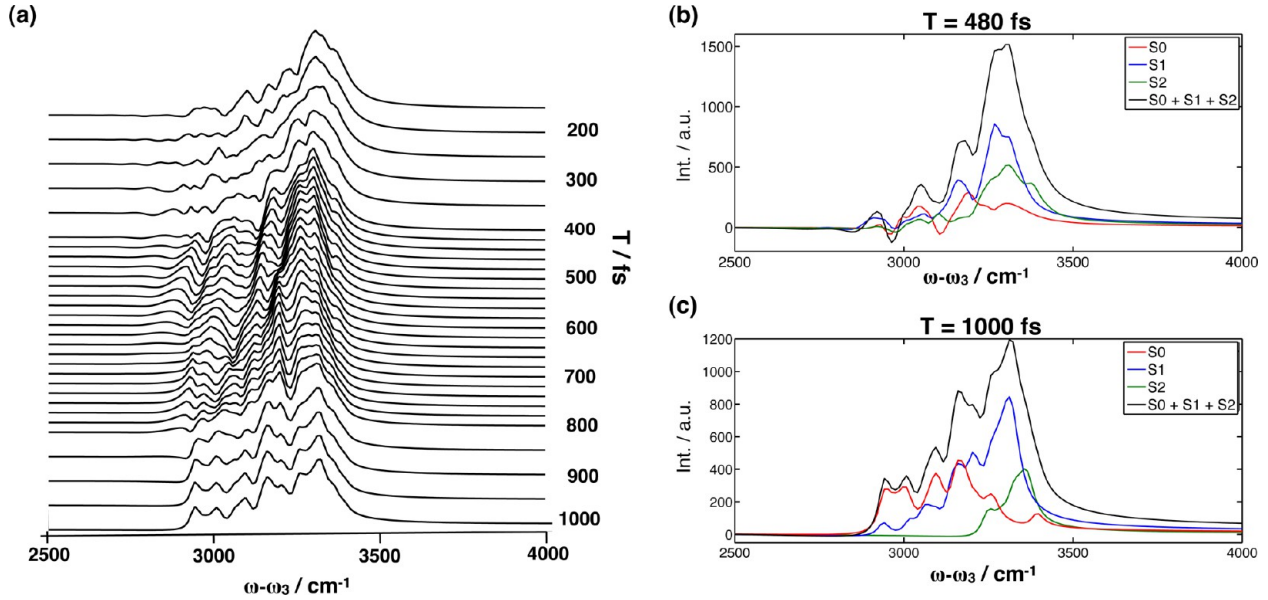

Figure 8. (a) SRS signal (eq 2) of C−H-stretch vibrations averaged over 32 trajectories. Contributions of the different populated electronic states at T = 480 fs and T = 1000 fs are depicted in panels b and c.

matter dynamics. Inspection of Figures 6 and 7 reveals that the dynamics of C−H-stretch vibrations of the $\pi\pi^* \rightarrow n_O\pi^*$ relaxation induce the largest frequency changes and accordingly require the shortest pulses. The spanned ∼500 cm^{-1} bandwidth along the Δ axis can be obtained by pulses on the order of 25 fs, readily available in the optical regime.

4.4. Ensemble Averaged SRS Signal of Uracil. In Figure 8a, we present the SRS signal of uracil averaged over 32 trajectories. We focus on C−H stretch vibrations as they act as local probes and respond instantaneously to distortions in ring planarity required to reach the CoIn structures (see section 4.3.1). At early delay times (T = 100 fs), we identify a single broad band (fwhm ≈ 200 cm^{-1}) centered at $\omega-\omega_3$ = 3323 cm^{-1} which does not allow one to resolve the individual C−H modes, as commonly observed for high-frequency C−H and N−H vibrations.[79] With increased delay time T = [100; 300] fs, the band shows an ultrafast red shift of $\Delta\omega-\omega_3$ = 15 cm^{-1} which can be assigned to ultrafast $S_2 \rightarrow S_1$ population transfer (compare Figure 3c). Further increase of T (300−700 fs) leads to the buildup of a pronounced shoulder at the red wing of the band of C−H modes which reaches just below 3000 cm^{-1} and obeys the characteristic dispersive peak shape of nonexponential CoIn induced dynamics. This transient modulation reflects the required out-of-plane deformations of the ring π system required to reach S_2/S_1 CoIn structures and more pronounced for S_1/S_0 CoIn structures (see Figures 4c and 5c). Comparison of the C−H vibrational spectra of ethylene and ethane[80,81] as prototype sp^2 and sp^3 species, respectively, reveals a red shift of C−H modes of ∼120 cm^{-1}, in agreement with the red shift of transient signatures. The SRS signal of C−H modes thus provides a sensitive local probe of out-of-plane deformations and the local hybridization state of carbon atoms even in the averaged signal. A further increase in T (700−1000 fs) leads to a decay of the dispersive signatures, and absorptive features due to band narrowing can be identified. Nevertheless, due to the substantial population of all three electronic states, a broad band reaching from ∼2950 to 3370 cm^{-1} persists.

In Figure 8b and c, we decompose the averaged SRS signal into the composite contributions of the individual electronic states for T = 480 and 1000 fs, respectively (18.8% S_0, 46.8% S_1, and 34.4% S_2 for T = 480 fs). At both delay times, we observe a strong spectral overlap of the different product channels which each obey a broad distribution. The dispersive line shapes in the total signal at T = 480 fs around $\omega-\omega_3 \approx$ 3000 cm^{-1} predominantly arise from S_0. Note that due to the path integral in eq 6 trajectories eventually relaxing into S_0 but still in S_1 or S_2 at T = 480 fs have dispersive contributions prior to their hopping event and cause the S_1 and S_2 contributions to this spectral feature. The S_1 and S_2 contributions to the SRS signal strongly overlap at $\omega-\omega_3 \approx$ 3300 cm^{-1}, but S_1 already shows a pronounced double peak structure. S_0 contributions are minor in this spectral region.

For T = 1000 fs (Figure 8c), the individual state contributions appear more separated, but substantial overlap persists. The S_2 contributions to the SRS signal appear with highest frequencies (green line) and resemble a single peak contributing to the signal. The S_1 contributions are most pronounced at $\omega-\omega_3$ = 3312 cm^{-1} and induce the main peak in the total SRS signal, while the red-shifted double peak shoulder until $\omega-\omega_3 \approx$ 3100 cm^{-1} is caused by S_1 and S_0 contributions. Around 3000 cm^{-1}, the dominant contributions to the SRS signal arise from the S_0 state.

5. CONCLUSIONS AND DISCUSSION

We have implemented a simulation protocol for frequency gated SRS signals which allows one to derive the system dynamics directly from ab initio on-the-fly simulations and tracks the system dynamics over nonadiabatic relaxation events in the vicinity of CoIns. The protocol is especially suited for high-frequency spectator modes where the excited state Hessian is reconstructed for the desired modes only using a mode tracking procedure. This allows one to decouple the numerical effort from system size and makes the excited state vibrational dynamics of medium sized molecules accessible for ab initio simulations.

The semiclassical signal expressions are derived microscopically from loop diagrams and fully account for the time/frequency resolution limits imposed by the Fourier uncertainty.

The delay time T and the frequency resolution of the detection axis $\omega-\omega_3$ are independent experimental knobs, and the SRS signal at time T does not represent a snapshot of the system dynamics. Matter dynamics induces a chirp contribution to the SRS signal which directly shows up in the evolution of the width of the resonances and induces dispersive line shapes in the SRS signals. Analysis of the Δ-dispersed signals demonstrates these matter-chirp contributions to the signal and allows one to estimate the optimal laser pulse bandwidth in SRS experiments. In the averaged signal, we observe a strong overlap of the different relaxation channels where the individual C−H modes are not resolved. Nevertheless, the system dynamics can still be resolved at the appropriate detection frequencies. Most importantly, characteristic dispersive line shapes indicative of nonexponential CoIn induced dynamics are clearly identified in the SRS signal around T = 500 fs. The results demonstrate that detection of C−H modes offers a valuable local probe of out-of-plane deformations of the π system and the local hybridization state of their adjacent carbon atoms.

To enhance the resolution of overlapping relaxation channels monitored in the SRS signal of C−H stretch vibrations, 2D variants with FSRS[82,83] or IR probes[84] could be of immanent value to spread the detection in two dimensions. This allows one to detect the detailed energy flows within the molecular systems, anharmonic couplings of C−H vibrations together with their vibrational relaxation. The low-frequency modes of the reaction coordinate and their coherence can be probed by sidebands of the high-frequency Raman spectrum of C−H modes with time-dependent line shapes which then function as direct reporter modes. Moreover, single molecule detection[40,41] could open exciting possibilities to detect the subpopulations and quantum trajectories of individual molecules which together add up to the averaged SRS signal. This requires novel detection strategies like vibrational detection or X-ray diffraction, which is sensitive to changes in electron density distribution. The commonly employed single molecule fluorescence detection is inapplicable due to the short lifetimes of the reactive species, which limits the quantum yield.

APPENDIX

1. The UV-Pump Stimulated Raman-Probe Signals with Joint Time/Frequency Representation of the Field

Both presented signal expressions use a joint time−frequency representation of the pulse that may help the analysis.

1.1. The von Neumann Representation. The von Neumann transformation of the field converts a discrete complex-valued signal from the time or the frequency domain into a two-dimensional joint time−frequency grid.[78] The two-dimensional grid that represents an arbitrary pulse is usually expressed in terms of complex Gaussians:

$$\alpha_{\omega_n t_m}(\omega) = \left(\frac{2\alpha}{\pi}\right)^{1/4} \exp[-\alpha(\omega-\omega_n)^2 - it_m(\omega-\omega_n)] \tag{21}$$

Transforming the Gaussian basis into the time-domain gives

$$\alpha_{\omega_n t_m}(t) = \left(\frac{1}{2\pi\alpha}\right)^{1/4} \exp\left[-\frac{1}{4\alpha}(t-t_m)^2 - it\omega_n\right] \tag{22}$$

The points (ω_n, t_m) of the von Neumann plane are distributed uniformly over the complete frequency range Ω_s and T_s. The step size in frequency and time are defined as $\Delta\omega = \Omega_s/k$ and $\Delta t = T_s/k$, where k is the number of points, which is the same for both time and frequency. This means that the values of the grid are given by $\omega_n = \omega_{min} + (n - 1/2)\Delta\omega$ and $t_m = -T_s/2 + (m - 1/2)\Delta t$ with $m, n = 1...k$.

For an arbitrary pulse depending on the choice of time or frequency domain, we associate the following two-dimensional expansion:

$$E(\omega) = \sum_{n,m} \tilde{Q}_{\omega_n t_m} \alpha_{\omega_n t_m}(\omega) \tag{23}$$

$$E(t) = \sum_{n,m} \tilde{Q}_{\omega_n t_m} \alpha_{\omega_n t_m}(t) \tag{24}$$

where the complex valued von Neumann coefficients are evaluated as

$$\tilde{Q}_{\omega_n t_m} = \sum_{i,j} S^{-1}_{(nm,ij)} \int \alpha^*_{\omega_i t_j}(\omega)\, E(\omega)\, d\omega \tag{25}$$

$$= \sum_{i,j} S^{-1}_{(nm,ij)} \int \alpha^*_{\omega_i t_j}(t)\, E(t)\, dt \tag{26}$$

$$= \sum_{i,j} S^{-1}_{(nm,ij)} \langle \alpha_{\omega_i t_j} | E \rangle \tag{27}$$

where the scalar product is defined as $\langle a|b\rangle = \int a^*(\omega)\, b(\omega)\, d\omega$. The overlap matrix $S_{(nm,ij)} = \langle \alpha_{\omega_n t_m} | \alpha_{\omega_i t_j} \rangle$ for the Gaussian basis set is given by

$$S_{(nm,ij)} = \sqrt{\frac{2\alpha}{\pi}} \exp\left[-\frac{\alpha}{2}(\omega_n-\omega_i)^2 - \frac{1}{8\alpha}(t_j-t_m)^2 + \frac{i}{2}(\omega_i-\omega_n)(t_j+t_m)\right] \tag{28}$$

The widths of the Gaussians are determined by the requirement that the standard deviation is $\Omega_s/(2\pi N)^{1/2}$, corresponding to

$$\alpha = 2\pi N/(2\Omega_s)^2 = Ts/2\Omega_s \tag{29}$$

Using the von Neumann representation (Figure 9) for the probe pulse $\mathcal{E}_2$, the frequency gated SRS signal can be expressed as

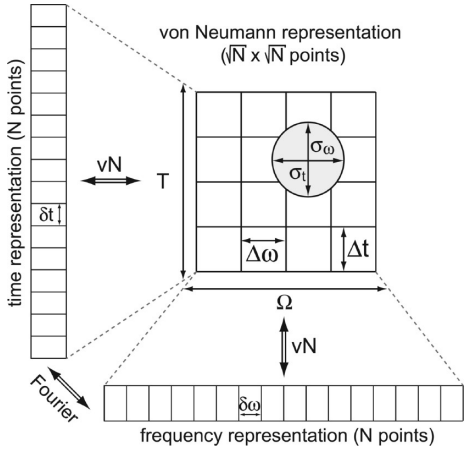

Figure 9. T and Ω in the figure is equivalent to T_s and Ω_s in the text. von Neumann plane (Reprinted with permission from ref 78. Copyright 2007 Optical Society of America).

dx.doi.org/10.1021/ct401012u | J. Chem. Theory Comput. 2014, 10, 1172−1188

$$S_{\mathrm{SRS}}(\omega-\omega_3, T) = \mathcal{I}\mathcal{E}_2^* \sum_{n,m} \tilde{Q}_{\omega_n t_m} \tilde{S}_{\mathrm{SRS}}(\omega-\omega_3, T; \omega_n, t_m) \tag{30}$$

where the bare signal is given by the two diagrams $\tilde{S}_{\mathrm{SRS}}(\omega-\omega_3, T; \omega_n, t_m) = \tilde{S}^{(i)}_{\mathrm{SRS}}(\omega-\omega_3, T; \omega_n, t_m) + \tilde{S}^{(ii)}_{\mathrm{SRS}}(\omega-\omega_3, T; \omega_n, t_m)$.

$$\begin{aligned}\tilde{S}^{(i)}_{\mathrm{SRS}}&(\omega-\omega_3, T; \omega_n, t_m) \\ &= \frac{2}{\hbar}|\mathcal{E}_1|^2|\mathcal{E}_3|^2 \int_{-\infty}^{\infty} \mathrm{d}t \int_{-\infty}^{t} \mathrm{d}\tau_3\, \alpha_{\omega_n t_m}(\tau_3 - T) \\ &\quad \times \langle V_e G^\dagger(\tau_3, 0)\alpha_n G^\dagger(t, \tau_3)\alpha_n G(t, 0) V_e^\dagger\rangle\, e^{i(\omega-\omega_3)(t-T)}\end{aligned} \tag{31}$$

$$\begin{aligned}\tilde{S}^{(ii)}_{\mathrm{SRS}}&(\omega-\omega_3, T; \omega_n, t_m) \\ &= \frac{2}{\hbar}|\mathcal{E}_1|^2|\mathcal{E}_3|^2 \int_{-\infty}^{\infty} \mathrm{d}t \int_{-\infty}^{t} \mathrm{d}\tau_3\, \alpha_{\omega_n t_m}(\tau_3 - T) \\ &\quad \times \langle V_e G^\dagger(t, 0)\alpha_n G(t, \tau_3)\alpha_n G(\tau_3, 0) V_e^\dagger\rangle\, e^{i(\omega-\omega_3)(t-T)}\end{aligned} \tag{32}$$

and we have assumed impulsive UV excitation $\mathcal{E}_1(\tau) = \mathcal{E}_1\delta(\tau)$. Here, the matter correlation function is expressed in the time domain, which is appropriate for the slow dynamics.

The n,m term in the summation in eq 30 represents the contribution of the ω_n, t_m component of the probe field to the signal detected at ω, T. It is determined by both the field $\tilde{Q}$ and the matter response $\tilde{S}$.

The respective frequency domain matter correlation function expressions read

$$\begin{aligned}\tilde{S}^{(i)}_{\mathrm{SRS}}&(\omega-\omega_3, T; \omega_n, t_m) \\ &= \frac{4\pi}{\hbar}|\mathcal{E}_1|^2 \int_{-\infty}^{\infty} \frac{\mathrm{d}\omega_1}{2\pi}\frac{\mathrm{d}\Delta}{2\pi}\, \alpha_{\omega_n t_m}(\omega + \Delta) \\ &\quad \times \langle V_e G^\dagger(\omega_g + \omega_1)\, \alpha_n G^\dagger(\omega_g + \omega_1 - \omega + \omega_3 - \Delta) \\ &\quad \alpha_n G(\omega_g + \omega_1 - \Delta)\, V_e^\dagger\rangle\, e^{i\Delta T}\end{aligned} \tag{33}$$

$$\begin{aligned}\tilde{S}^{(ii)}_{\mathrm{SRS}}&(\omega-\omega_3, T; \omega_n, t_m) \\ &= \frac{4\pi}{\hbar}|\mathcal{E}_1|^2 \int_{-\infty}^{\infty} \frac{\mathrm{d}\omega_1}{2\pi}\frac{\mathrm{d}\Delta}{2\pi}\, \alpha_{\omega_n t_m}(\omega + \Delta) \\ &\quad \times \langle V_e G^\dagger(\omega_g + \omega_1)\, \alpha_n G(\omega_g + \omega-\omega_3 + \omega_1) \\ &\quad \alpha_n G(\omega_g + \omega_1 - \Delta)\, V_e^\dagger\rangle\, e^{i\Delta T}\end{aligned} \tag{34}$$

which is more appropriate for fast system dynamics.

1.2. The Wigner Representation. The von Neumann representation of optical pulses can be connected to another mixed time−frequency representation—the Wigner representation. The Wigner spectrogram for an arbitrary pulse $\mathcal{E}(t)$ is defined by

$$W(\omega, t) = \int_{-\infty}^{\infty} \mathrm{d}\tau\, \mathcal{E}^*(t - \tau/2)\, \mathcal{E}(t + \tau/2)\, e^{i\omega\tau} \tag{35}$$

or alternatively in the frequency domain

$$W(\omega, t) = \int_{-\infty}^{\infty} \mathrm{d}\Omega\, \mathcal{E}^*(\omega - \Omega/2)\, \mathcal{E}(\omega + \Omega/2)\, e^{-i\Omega t} \tag{36}$$

By taking into account eqs 21 and 22, we obtain

$$W(\omega, t) = \sum_{n,m,i,j} \tilde{Q}^*_{\omega_n t_m} \tilde{Q}_{\omega_i t_j} S_{(nm)(ij)} \mathcal{W}_{(nm)(ij)}(\omega, t) \tag{37}$$

where $S_{(nm)(ij)}$ is given by eq 28 and $\mathcal{W}_{(nm)(ij)}(\omega, t)$ is a Wigner spectrogram for the Gaussian basis

$$\begin{aligned}\mathcal{W}_{(nm)(ij)}(\omega, t) &= \sqrt{\frac{2\pi}{\alpha}} \\ &\exp\left[-\frac{1}{2\alpha}\left(t + \frac{t_m + t_j}{2} - i\alpha(\omega_n - \omega_i)\right)^2\right] \\ &\exp\left[-2\alpha\left(\omega - \frac{\omega_n + \omega_i}{2} - \frac{i}{4\alpha}(t_m - t_j)\right)^2\right]\end{aligned} \tag{38}$$

The SRS signal in the Wigner representation is given by

$$\begin{aligned}S^{(i)}_{\mathrm{SRS}}&(\omega - \omega_3, T) = \mathcal{I}\frac{2}{\hbar}\int_{-\infty}^{\infty} \mathrm{d}t\, \mathrm{d}t_1\, \mathrm{d}\Delta/2\pi W_2(\omega, t) \\ &\times W_1(\omega_1, t_1)\, e^{i\Delta T}\langle V_e G^\dagger(\omega_g + \omega_1) \\ &\alpha_n G^\dagger(\omega_g + \omega_1 - \omega + \omega_3 - \Delta) \\ &\alpha_n G(\omega_g + \omega_1 - \Delta) V_e^\dagger\rangle\end{aligned} \tag{39}$$

$$\begin{aligned}S^{(ii)}_{\mathrm{SRS}}&(\omega-\omega_3, T) = \mathcal{I}\frac{2}{\hbar}\int_{-\infty}^{\infty} \mathrm{d}t\, \mathrm{d}t_1\, \mathrm{d}\Delta/2\pi W_2(\omega, t) \\ &\times W_1(\omega_1, t_1)\, e^{i\Delta T}\langle V_e G^\dagger(\omega_g + \omega_1) \\ &\alpha_n G(\omega_g + \omega-\omega_3 + \omega_1)\, \alpha_n G(\omega_g + \omega_1 - \Delta) V_e^\dagger\rangle\, e^{i\Delta T}\end{aligned} \tag{40}$$

AUTHOR INFORMATION

Corresponding Authors

*E-mail: bfingerh@uci.edu.
*E-mail: kdorfman@uci.edu.
*E-mail: smukamel@uci.edu.

Notes

The authors declare no competing financial interest.

ACKNOWLEDGMENTS

We gratefully acknowledge the support of the National Science Foundation (NSF) through Grant No. CHE-1058791, and computations were supported by Grant No. CHE-0840513, the Chemical Sciences, Geosciences and Biosciences Division, Office of Basic Energy Sciences, Office of Science, and (U.S.) Department of Energy (DOE), National Institutes of Health (NIH) Grant No. GM-59230. The postdoctoral fellowship of K.E.D. was funded by DOE. B.P.F. gratefully acknowledges support from the Alexander-von-Humboldt Foundation through the Feodor-Lynen program.

REFERENCES

(1) Mohammed, O. F.; Pines, D.; Dreyer, J.; Pines, E.; Nibbering, E. T. J. *Science* **2005**, *310*, 83−86.
(2) Schreier, W. J.; Schrader, T. E.; Koller, F. O.; Gilch, P.; Crespo-Hernández, C. E.; Swaminathan, V. N.; Carell, T.; Zinth, W.; Kohler, B. *Science* **2007**, *315*, 625−9.
(3) Kukura, P.; McCamant, D. W.; Mathies, R. A. *Annu. Rev. Phys. Chem.* **2007**, *58*, 461−488.
(4) Kuramochi, H.; Takeuchi, S.; Tahara, T. *J. Phys. Chem. Lett.* **2012**, *3*, 2025−2029.
(5) Kukura, P.; McCamant, D. W.; Yoon, S.; Wandschneider, D. B.; Mathies, R. A. *Science* **2005**, *310*, 1006−1009.
(6) Takeuchi, S.; Ruhman, S.; Tsuneda, T.; Chiba, M.; Taketsugu, T.; Tahara, T. *Science* **2008**, *322*, 1073−1077.

(7) Liebel, M.; Schnedermann, C.; Kukura, P. 2013, ArXiv e-prints: 1309.7929.
(8) McCamant, D. W.; Kukura, P.; Yoon, S.; Mathies, R. A. *Rev. Sci. Instrum.* **2004**, *75*, 4971−4980.
(9) Kraack, J. P.; Wand, A.; Buckup, T.; Motzkus, M.; Ruhman, S. *Phys. Chem. Chem. Phys.* **2013**, *15*, 14487−14501.
(10) Fang, C.; Frontiera, R. R.; Tran, R.; Mathies, R. A. *Nature* **2009**, *462*, 200−4.
(11) Dorfman, K. E.; Fingerhut, B. P.; Mukamel, S. *Phys. Chem. Chem. Phys.* **2013**, *15*, 12348−12359.
(12) Dorfman, K. E.; Fingerhut, B. P.; Mukamel, S. *J. Chem. Phys.* **2013**, *139*, 124113.
(13) Fingerhut, B. P.; Dorfman, K. E.; Mukamel, S. *J. Phys. Chem. Lett.* **2013**, *4*, 1933−1942.
(14) Barbatti, M.; Granucci, G.; Persico, M.; Ruckenbauer, M.; Vazdar, M.; Eckert-Maksić, M.; Lischka, H. *J. Photochem. Photobiol. A* **2007**, *190*, 228−240.
(15) Fingerhut, B. P.; Oesterling, S.; Haiser, K.; Heil, K.; Glas, A.; Schreier, W. J.; Zinth, W.; Carell, T.; de Vivie-Riedle, R. *J. Chem. Phys.* **2012**, *136*, 204307.
(16) Reiher, M.; Neugebauer, J. *J. Chem. Phys.* **2003**, *118*, 1634−1641.
(17) Mukamel, S.; Biggs, J. D. *J. Chem. Phys.* **2011**, *134*, 161101.
(18) Umapathy, S.; Lakshmanna, A.; Mallick, B. *J. Raman Spectrosc.* **2009**, *40*, 235−237.
(19) Middleton, C. T.; de La Harpe, K.; Su, C.; Law, Y. K.; Crespo-Hernández, C. E.; Kohler, B. *Annu. Rev. Phys. Chem.* **2009**, *60*, 217−39.
(20) Crespo-Hernández, C. E.; Cohen, B.; Hare, P. M.; Kohler, B. *Chem. Rev.* **2004**, *104*, 1977−2020.
(21) Schreier, W. J.; Kubon, J.; Regner, N.; Haiser, K.; Schrader, T. E.; Zinth, W.; Clivio, P.; Gilch, P. *J. Am. Chem. Soc.* **2009**, *131*, 5038−9.
(22) Crespo-Hernández, C. E.; Cohen, B.; Kohler, B. *Nature* **2005**, *436*, 1141−4.
(23) Markovitsi, D.; Talbot, F.; Gustavsson, T.; Onidas, D.; Lazzarotto, E.; Marguet, S. *Nature* **2006**, *441*, E7 discussion E8.
(24) Vayá, I.; Gustavsson, T.; Miannay, F.-A.; Douki, T.; Markovitsi, D. *J. Am. Chem. Soc.* **2010**, *132*, 11834−5.
(25) Selig, U.; Schleussner, C.-F.; Foerster, M.; Langhojer, F.; Nuernberger, P.; Brixner, T. *Opt. Lett.* **2010**, *35*, 4178−4180.
(26) West, B. A.; Moran, A. M. *J. Phys. Chem. Lett.* **2012**, *3*, 2575−2581.
(27) Krebs, N.; Pugliesi, I.; Riedle, E. *Appl. Sci.* **2013**, *3*, 153−167.
(28) Satzger, H.; Townsend, D.; Zgierski, M. Z.; Patchkovskii, S.; Ullrich, S.; Stolow, A. *Proc. Natl. Acad. Sci. U. S. A.* **2006**, *103*, 10196−201.
(29) Canuel, C.; Mons, M.; Piuzzi, F.; Tardivel, B.; Dimicoli, I.; Elhanine, M. *J. Chem. Phys.* **2005**, *122*, 074316.
(30) Ullrich, S.; Schultz, T.; Zgierski, M. Z.; Stolow, A. *Phys. Chem. Chem. Phys.* **2004**, *6*, 2796−2801.
(31) Hare, P. M.; Crespo-Hernández, C. E.; Kohler, B. *Proc. Natl. Acad. Sci. U. S. A.* **2007**, *104*, 435−440.
(32) Ismail, N.; Blancafort, L.; Olivucci, M.; Kohler, B.; Robb, M. A. *J. Am. Chem. Soc.* **2002**, *124*, 6818−6819.
(33) Matsika, S. *J. Phys. Chem. A* **2004**, *108*, 7584−7590.
(34) Asturiol, D.; Lasorne, B.; Robb, M. A.; Blancafort, L. *J. Phys. Chem. A* **2009**, *113*, 10211−10218.
(35) Gustavsson, T.; Bányász, A.; Lazzarotto, E.; Markovitsi, D.; Scalmani, G.; Frisch, M. J.; Barone, V.; Improta, R. *J. Am. Chem. Soc.* **2006**, *128*, 607−19.
(36) Hudock, H. R.; Levine, B. G.; Thompson, A. L.; Satzger, H.; Townsend, D.; Gador, N.; Stolow, A.; Martinez, T. J. *J. Phys. Chem. A* **2007**, *111*, 8500−8508.
(37) Nachtigallová, D.; Aquino, A. J. A.; Szymczak, J. J.; Barbatti, M.; Hobza, P.; Lischka, H. *J. Phys. Chem. A* **2011**, *115*, 5247−5255.
(38) Lan, Z.; Fabiano, E.; Thiel, W. *J. Phys. Chem. B* **2009**, *113*, 3548−3555.
(39) McFarland, B. K. et al. 2013, ArXiv e-prints: 1301.3104.
(40) van Dijk, E. M. H. P.; Hernando, J.; García-López, J.-J.; Crego-Calama, M.; Reinhoudt, D. N.; Kuipers, L.; García-Parajó, M. F.; van Hulst, N. F. *Phys. Rev. Lett.* **2005**, *94*, 078302.
(41) Brinks, D.; Stefani, F. D.; Kulzer, F.; Hildner, R.; Taminiau, T. H.; Avlasevich, Y.; Mu, K. *Nature* **2010**, *465*, 905−909.
(42) Schneider, R.; Domcke, W. *Chem. Phys. Lett.* **1988**, *150*, 235−242.
(43) Raab, A.; Worth, G. A.; Meyer, H.-D.; Cederbaum, L. S. *J. Chem. Phys.* **1999**, *110*, 936−946.
(44) Peon, J.; Zewail, A. H. *Chem. Phys. Lett.* **2001**, *348*, 255−262.
(45) Mendive-Tapia, D.; Lasorne, B.; Worth, G. A.; Bearpark, M. J.; Robb, M. A. *Phys. Chem. Chem. Phys.* **2010**, *12*, 15725−15733.
(46) Hamm, P.; Helbing, J.; Bredenbeck, J. *Chem. Phys.* **2006**, *323*, 54−65.
(47) Sailer, C. F.; Thallmair, S.; Fingerhut, B. P.; Nolte, C.; Ammer, J.; Mayr, H.; Pugliesi, I.; de Vivie-Riedle, R.; Riedle, E. *ChemPhysChem* **2013**, *14*, 1423−1437.
(48) Chernyak, V.; Mukamel, S. *J. Chem. Phys.* **1996**, *105*, 4565−4583.
(49) McCamant, D. W. *J. Phys. Chem. B* **2011**, *115*, 9299−9305.
(50) Weiner, A. M. *Opt. Commun.* **2011**, *284*, 3669−3692.
(51) Tully, J. C. *J. Chem. Phys.* **1990**, *93*, 1061.
(52) Barbatti, M.; Shepard, R.; Lischka, H. In *Conical Intersections: Theory, Computation and Experiment*; Domcke, W., Yarkony, D. R., Koppel, H., Eds.; World Scientific: Singapore, 2011; pp 415−462.
(53) Warshel, A. *Nature* **1976**, *260*, 679−683.
(54) Werner, H.-J. et al. MOLPRO, version 2009.1, a package of ab initio programs. http://www.molpro.net.
(55) Buchner, M.; Ladanyi, B. M.; Stratt, R. M. *J. Chem. Phys.* **1992**, *97*, 8522−8535.
(56) Keyes, T. *J. Phys. Chem. A* **1997**, *101*, 2921−2930.
(57) Moore, P.; Keyes, T. *J. Chem. Phys.* **1994**, *100*, 6709−6717.
(58) Nguyen, P. H.; Stock, G. *J. Chem. Phys.* **2003**, *119*, 11350−11358.
(59) Bastida, A.; Soler, M. A.; Zuniga, J.; Requena, A.; Kalstein, A.; Fernandez-Alberti, S. *J. Chem. Phys.* **2010**, *132*, 224501.
(60) Long, D. A. *The Raman Effect−A Unified Treatment of the Theory of Raman Scattering by Molecules*; John Wiley & Sons, Ltd: New York, 2002; pp 85−152.
(61) Neugebauer, J.; Reiher, M.; Kind, C.; Hess, B. A. *J. Comput. Chem.* **2002**, *23*, 895−910.
(62) Swope, W. C.; Andersen, H. C.; Berens, P. H.; Wilson, K. R. *J. Chem. Phys.* **1982**, *76*, 637−649.
(63) Hammes-Schiffer, S.; Tully, J. C. *J. Chem. Phys.* **1994**, *101*, 4657−4667.
(64) Butcher, J. C. *J. Assoc. Comput. Mach.* **1965**, *12*, 124−135.
(65) Serrano-Andrés, L.; Merchán, M. *J. Photochem. Photobiol. C* **2009**, *10*, 21−32.
(66) Kistler, K. A.; Matsika, S. *J. Chem. Phys.* **2008**, *128*, 215102.
(67) Delchev, V. B.; Sobolewski, A.; Domcke, W. *Phys. Chem. Chem. Phys.* **2010**, *12*, 5007−5015.
(68) Barbatti, M.; Aquino, A. J. A.; Szymczak, J. J.; Nachtigallová, D.; Hobza, P.; Lischka, H. *Proc. Natl. Acad. Sci. U. S. A.* **2010**, *107*, 21453−21458.
(69) Finley, J.; Malmqvist, P.-A.; Roos, B. O.; Serrano-Andrés, L. *Chem. Phys. Lett.* **1998**, *288*, 299−306.
(70) Celani, P.; Werner, H.-J. *J. Chem. Phys.* **2003**, *119*, 5044−5057.
(71) Roos, B. O.; Andersson, K. *Chem. Phys. Lett.* **1995**, *245*, 215−223.
(72) Bacskay, G. B.; Saebo, S.; Taylor, P. R. *Chem. Phys.* **1984**, *90*, 215−224.
(73) Clark, L. B.; Tinoco, I. *J. Am. Chem. Soc.* **1965**, *87*, 11−15.
(74) Epifanovsky, E.; Kowalski, K.; Fan, P.-D.; Valiev, M.; Matsika, S.; Krylov, A. I. *J. Phys. Chem. A* **2008**, *112*, 9983−9992.
(75) Szymczak, J. J.; Barbatti, M.; Lischka, H. *Int. J. Quantum Chem.* **2011**, *111*, 3307−3315.
(76) Tao, H.; Levine, B. G.; Martnez, T. J. *J. Phys. Chem. A* **2009**, *113*, 13656−13662.

(77) Yamazaki, S.; Taketsugu, T. *J. Phys. Chem. A* **2012**, *116*, 491−503.
(78) Fechner, S.; Dimler, F.; Brixner, T.; Gerber, G.; Tannor, D. J. *Opt. Express* **2007**, *15*, 15387−15401.
(79) Colarusso, P.; Zhang, K.; Guo, B.; Bernath, P. F. *Chem. Phys. Lett.* **1997**, *269*, 39−48.
(80) NIST Standard Reference Database 69: NIST Chemistry WebBook. http://webbook.nist.gov/cgi/cbook.cgi?ID=74-84-0 (accessed Nov 21, 2013).
(81) NIST Standard Reference Database 69: NIST Chemistry WebBook. http://webbook.nist.gov/cgi/cbook.cgi?ID=74-85-1 (accessed Nov 21, 2013).
(82) Wilson, K. C.; Lyons, B.; Mehlenbacher, R.; Sabatini, R.; McCamant, D. W. *J. Chem. Phys.* **2009**, *131*, 214502.
(83) Dunlap, B.; Wilson, K. C.; McCamant, D. W. *J. Phys. Chem. A* **2013**, *117*, 6205−6216.
(84) Lynch, M. S.; Slenkamp, K. M.; Cheng, M.; Khalil, M. *J. Phys. Chem. A* **2012**, *116*, 7023−7032.